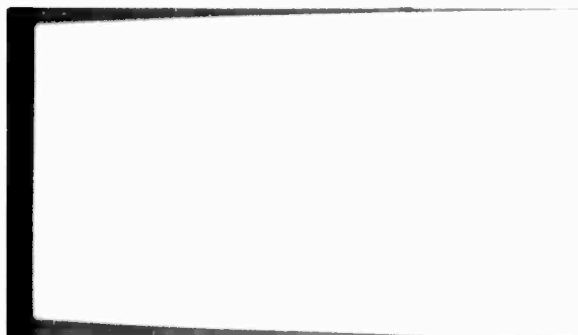


AD 730069



**DISTRIBUTION STATEMENT A**  
Approved for public release;  
Distribution Unlimited

**DDC**  
**RECEIVED**  
SEP 28 1971  
**RECEIVED**  
**B**

Reproduced by  
**NATIONAL TECHNICAL  
INFORMATION SERVICE**  
Springfield, Va. 22151

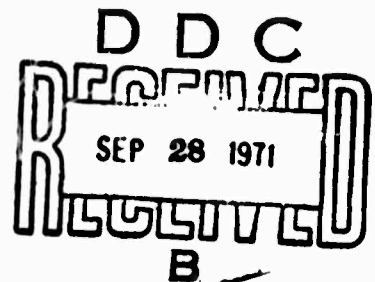
**BEST  
AVAILABLE COPY**

**HIGH-EFFICIENCY, SINGLE-  
FREQUENCY LASER  
AND MODULATOR STUDY**

**Semiannual Technical Report**

**LMSC-D179854**

**30 April 1971**



**R. C. Ohlmann, W. Culshaw, K. K. Chow, H. V. Hance,  
W. B. Leonard, and J. Kannelaud**

**ARPA Order No. 306**

**Contract No. N00014-71-C-0049**

**Program Code 421**

**Effective Date of Contract: 1 September 1970**

**Expiration Date: 30 September 1971**

**Amount: \$139,100**

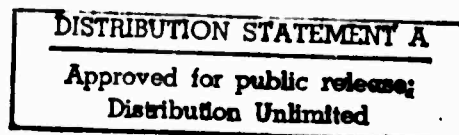
**Scientific Officer: Director, Physics Programs,  
Physical Sciences Division**

**Office of Naval Research, Arlington, Va. 22217**

**Principal Investigator: R. C. Ohlmann (415) 324-3311, ext. 45275**

**Sponsored by the  
Advanced Research Projects Agency  
ARPA Order No. 306**

**The views and conclusions contained in this document  
are those of the authors and should not be interpreted  
as necessarily representing the official policies, either  
expressed or implied, of the Advanced Research Proj-  
ects Agency or the U.S. Government.**



## DOCUMENT CONTROL DATA - R &amp; D

(Security classification of title, body of abstract and indexing annotation must be entered when the overall report is classified)

1. ORIGINATING ACTIVITY (Corporate author) Lockheed Palo Alto Research Laboratory Lockheed Missiles & Space Company Palo Alto, Calif. 94304		2a. REPORT SECURITY CLASSIFICATION Unclassified	
		2b. GROUP	
3. REPORT TITLE HIGH-EFFICIENCY, SINGLE-FREQUENCY LASER AND MODULATOR STUDY			
4. DESCRIPTIVE NOTES (Type of report and inclusive dates) Semiannual Technical Report, 1 September 1970 - 31 March 1971			
5. AUTHOR(S) (First name, middle initial, last name) Robert C. Ohlmann et al.			
6. REPORT DATE 30 April 1971		7a. TOTAL NO. OF PAGES 58	7b. NO. OF REFS 7
8a. CONTRACT OR GRANT NO. N00014-71-C-0049		8a. ORIGINATOR'S REPORT NUMBER(S) LMSC-D179854	
b. PROJECT NO. ARPA Order No. 306			
c. Program Code No. 421		8b. OTHER REPORT NO(S) (Any other numbers that may be assigned this report)	
d.			
9. DISTRIBUTION STATEMENT Distribution of this document is unlimited.			
11. SUPPLEMENTARY NOTES None		12. SPONSORING MILITARY ACTIVITY Office of Naval Research, Physics Programs, Physical Sciences Division Arlington, Va. 22217	
13. ABSTRACT Theoretical and experimental studies on (1) mode filters for single-frequency Nd:YAG lasers, (2) wide-bandwidth optical modulators, and (3) laser communication systems and components are reported. Stable single-frequency output power of 0.2 W is obtained from a Nd:YAG laser by using a combination of a tilted etalon and a thin metallic film in the laser cavity. Detailed analyses have been made to reduce the insertion loss of mode filters to an absolute minimum so that efficiency can be increased. The electrooptic modulator uses a microwave interdigital filter structure and has a 1.2-GHz bandwidth. A new circuit design aimed at increasing modulation depth for a given rf power has been obtained. Theory indicates that the interferometric mode of modulation should increase efficiency over the birefringence mode; good experimental agreement has been obtained. Study of optical crystals has been initiated; no optical damage or beam distortion of LiNbO <sub>3</sub> was observed under continuous radiation of 14 kW/cm <sup>2</sup> green light when the crystal was at 180°C. Several laser communication system concepts and modulation formats have been selected for study. An annotated bibliography of these systems has been published.			

14.

KEY WORDS

**Lasers**  
**Solid-state lasers**  
**Neodymium**  
**Yttrium aluminum garnet**  
**Laser modes**  
**Laser communications**  
**Optical communications**  
**Wideband laser communications**  
**Laser modulators**  
**Optical modulators**  
**Electrooptic crystals**  
**Optical damage**  
**Laser communication system**

LINK A

LINK B

LINK C

ROLE

WT

ROLE

WT

ROLE

WT

## ABSTRACT

Theoretical and experimental studies on (1) mode filters for single-frequency Nd:YAG lasers, (2) wide-bandwidth optical modulators, and (3) laser communication systems and components are reported. Stable single-frequency output power of 0.2 W is obtained from a Nd:YAG laser by using a combination of a tilted etalon and a thin metallic film in the laser cavity. Detailed analyses have been made to reduce the insertion loss of mode filters to an absolute minimum so that efficiency can be increased. The electrooptic modulator uses a microwave interdigital filter structure and has a 1.2-GHz bandwidth. A new circuit design aimed at increasing modulation depth for a given rf power has been obtained. Theory indicates that the interferometric mode of modulation should increase efficiency over the birefringence mode; good experimental agreement has been obtained. Study of optical crystals has been initiated; no optical damage or beam distortion of LiNbO<sub>3</sub> was observed under continuous radiation of 14 kW/cm<sup>2</sup> green light when the crystal was at 180°C. Several laser communication system concepts and modulation formats have been selected for study. An annotated bibliography of these systems has been published.

## CONTENTS

Section		Page
	<b>ABSTRACT</b>	iii
1	<b>SUMMARY</b>	1-1
	1.1 Single-Frequency Nd:YAG Laser	1-2
	1.2 Wide-Bandwidth Optical Modulator	1-3
	1.3 List of Publications	1-6
2	<b>SINGLE-FREQUENCY Nd:YAG STUDIES</b>	2-1
	2.1 Introduction	2-1
	2.2 Tilted Fabry-Perot Etalon and Metallic Film Mode Selector	2-2
	2.3 Tilt Loss of Intracavity Fabry-Perot Etalons and Transverse Mode Control	2-5
	2.4 Double Metallic Film Mode Selector	2-14
	2.5 Laser Mirror With Variable Transmission Coefficient	2-19
	2.6 Further Investigations	2-20
3	<b>WIDE-BANDWIDTH OPTICAL MODULATOR</b>	3-1
	3.1 Study of the Modulator Circuit	3-1
	3.2 Interferometric Modulation Studies	3-15
	3.3 Electrooptic/Thermal Control Circuit	3-20
	3.4 Evaluation of Efficient Crystals	3-23
	3.5 Crystal Damage and Beam Profile Studies	3-23
	3.6 Future Plans	3-27
4	<b>REFERENCES</b>	4-1

## ILLUSTRATIONS

Figure		Page
1-1	1- to 2-GHz Modulator, Showing Details of Electrooptic Crystal Assembly for Automatic Electrooptical Bias	1-4
2-1	Tilted Fabry-Perot Etalon - Nichrome Film Mode Filter for Single-Frequency Nd:YAG Lasers	2-3
2-2	Distribution of the x-Component of the Electric Field Along the x-Axis; the Corresponding Angular Spectrum of Plane Waves; and the Parameters of the Tilted Fabry-Perot Etalon	2-7
2-3	Angular Plane Wave Spectra of Gaussian Beam Laser Resonator Modes, $B(k_x)$ Versus $k_x a$ , Where $k_x$ Is the x-Component of the Plane Wave Propagation Constant and $a$ Is the Beam Waist	2-8
2-4	Power Reflection Coefficients or Power Loss of the Tilted Fabry-Perot Etalon Versus Design Parameters for Laser Resonator Modes $TEM_{00}$ Through $TEM_{70}$	2-13
2-5	Double-Nichrome-Film Quartz Etalon Mode Filter for Single-Frequency Nd:YAG Lasers; Total Power Reflection Coefficient Versus Frequency Deviation From Resonance Condition	2-17
2-6	Designs for a Laser Output Mirror With a Continuously Variable Power Transmission Coefficient for Gain, Loss, and Saturation Parameter Measurements on Operating Nd:YAG Lasers	2-21
3-1	A Low-Pass Prototype Tchebyscheff Filter Circuit, Normalized to $\omega_1 = 1$ rad/sec and Generator Impedance $g_0 = 1 \Omega$	3-5
3-2	A Bandpass Filter Circuit After Transformation From Low-Pass Prototype Circuit	3-6
3-3	The Strip-Line Capacity-Loaded Interdigital Line Filter, Together With Its Generator and Load	3-7
3-4	An Approximate Equivalent Circuit for the Four-Element Capacity-Load Interdigital Line Filter	3-7
3-5	Approximate Equivalent Circuits of the Output Section of the Capacity-Loaded Interdigital Modulator	3-9
3-6	An Example of a Modulator Circuit Design: Effective Generator Impedance $19 \Omega$ , Load Impedance $19 \Omega$	3-14



Figure		Page
3-7	Block Diagram of the Automatic Electrooptical Bias Scheme	3-21
3-8	Extinction Patterns for Finished Electrooptic Crystals (apertures approximately 0.3 by 0.4 mm)	3-24
3-9	Measured TEM <sub>00</sub> Far-Field Beam Profile of an Argon Laser Output Showing the Gaussian Distribution	3-26
3-10	Measured Far-Field Beam Profile of an Argon Laser Output After Passing Through an Uncoated Focusing Lens	3-26
3-11	Measured Far-Field Beam Profile of an Argon Laser Output After Passing Through the Uncoated Focusing Lens and a LiNbO <sub>3</sub> Crystal	3-26

## TABLES

Table		Page
3-1	Transmission Modulation Characteristics of 0.5 by 0.5 by 7 mm LiNbO <sub>3</sub> Crystal at Various Drive Power Levels	3-17
3-2	Reflection Modulation Characteristics of 0.5 by 0.5 by 7 mm LiNbO <sub>3</sub> Crystal at Various Drive Power Levels	3-18

## Section 1 SUMMARY

The research effort reported here has the broad objective of contributing to the development of wide-bandwidth, high-data-rate laser communication systems. Specifically, the investigation is proceeding with three major tasks:

- (1) Design, fabrication, test, and operation of mode filters for Nd:YAG solid state lasers so as to obtain at least 1-W output power in a single mode (single frequency) at 1.06  $\mu\text{m}$
- (2) Analysis, design, fabrication, and test of a 1-GHz bandwidth optical modulator for 1.06- $\mu\text{m}$  radiation
- (3) Study and evaluation of laser communication system configurations and components that will lead to the formulation of realistic and appropriate objectives for component development

The selection of these tasks has been based on the concept that a realistic approach to the development of ultra-wideband laser communication systems must include developing a sufficiently stable and efficient laser source in the visible or near-infrared (a spectral region where fast, sensitive detectors are becoming available) and developing a broad-bandwidth efficient optical modulator. Tasks 1 and 2 attack these research and development problems by specific and promising theoretical and experimental techniques. There are other considerations to be taken into account for utilizing a laser communication system, including modulation formatting, communication efficiency, detector capability, and pointing and tracking. These problems are being approached under Task 3.

The progress on Tasks 1 and 2 is presented in depth in this report, with a brief summary given here. The principal progress on Task 3 has been an annotated bibliography on wideband laser communication systems and components entitled Wideband Laser Communications, LMSC Report N-JY-71-3/SB-71-1, which has been published and

distributed. In addition, a paper has been submitted to the International Telemetry Conference on modulation/demodulation techniques for optical systems.

### 1.1 SINGLE-FREQUENCY Nd:YAG LASER

The solid state laser using neodymium in yttrium aluminum garnet (Nd:YAG) has the greatest promise at present as an efficient modest-power source of coherent radiation and deserves development into a long-life, reliable space-qualified cw transmitter source. However, the output of the free-running cw laser is too noisy for use in a communication source; it exhibits both low-frequency perturbations and rf noise from the uncorrelated oscillation of many axial cavity modes within the broad frequency band (up to 50 GHz), where excess laser gain exists. Stable single-frequency operation is required to allow use of the laser as the source in a cw broadband communication system using a microwave subcarrier.

Our program under this task is to conduct both theoretical and experimental investigations into mode filters of three types: Fabry-Perot etalons, thin metallic films, and metallic gratings. These are placed within the laser cavity to provide frequency selectivity while having low insertion loss for one axial mode, and thus allow single-frequency operation of the Nd:YAG laser. During the first reporting period, a detailed theoretical analysis of the frequency spectrum and loss characteristics of these filters, both singly and in combination, was performed. The theory indicated that a good solution to the problem of efficiently providing 1-W output power in a single mode is the combination of a tilted Fabry-Perot etalon and a thin (50-100Å) metallic film mode selector. The advantage of this combination is that the best properties of each are utilized to obtain the required selectivity for the single-frequency operation of the Nd:YAG laser at the 1-W level of output power, and with the requisite low insertion loss. Preliminary experiments with this two-component mode filter in our present Nd:YAG laser gave 0.2-W single-frequency output with good stability, even without any feedback control on the cavity length. These investigations indicated that the single-frequency output from our present laser, pumped by a tungsten-iodine lamp in a spherical pump cavity, could be increased to the 0.5-W level or higher by the optimization of the  $TEM_{00}$  mode volume in the laser rod.

In the present reporting period, detailed considerations have been given to reducing the insertion loss of mode filters to an absolute minimum, which is essential for a 1% efficient Nd:YAG laser with 1-W output power. The tilt loss of intracavity Fabry-Perot etalons has been deduced by a more accurate theoretical method and optimum designs have been established. A knowledge of the laser operating parameters, such as gain, insertion losses, and the saturation parameter, is essential to the design of an efficient single-frequency laser, and methods of measuring these, utilizing designs of output laser mirrors with continuously variable transmission coefficients, were also developed. Some further work on the double metallic film mode filter was also done, with encouraging results with regard to potential low value of insertion loss. This mode filter is much more sensitive to laser perturbations, however, and it appears that practical use of it will be difficult.

In the next period, the design of our laser will be improved to reduce troublesome power fluctuations; more optimum filter designs will be established; and further work will be done on incorporation of a feedback control loop. Laser cavity designs with internal focusing elements to give optimum  $TEM_{00}$  mode volumes in the Nd:YAG rod will be evolved and used to obtain output powers of  $\sim 0.5$ -W from our present laser. Laser output mirrors with continuously variable transmission coefficients will be developed further and used in preliminary measurements of the operating parameters of the laser. Consideration will also be given to the early use of the more efficient potassium-rubidium lamp to pump our single-frequency Nd:YAG laser to obtain an output of 1 W at an efficiency of  $\sim 1\%$ .

## 1.2 WIDE-BANDWIDTH OPTICAL MODULATOR

The optical modulator presently under investigation employs an electrooptic crystal in a 1.2-GHz-bandwidth bandpass microwave interdigital filter structure, as shown in Fig. 1-1. Although excellent results have been obtained at LMSC using this device, with  $LiNbO_3$  as the modulating crystal, for the modulation of 0.6328- and 0.5145- $\mu m$  laser radiation, the efficiency of the device drops at longer wavelengths, as is true of all electrooptic modulators. Techniques are being developed for increasing the efficiency for modulation of the 1.06- $\mu m$  radiation from a Nd:YAG laser.

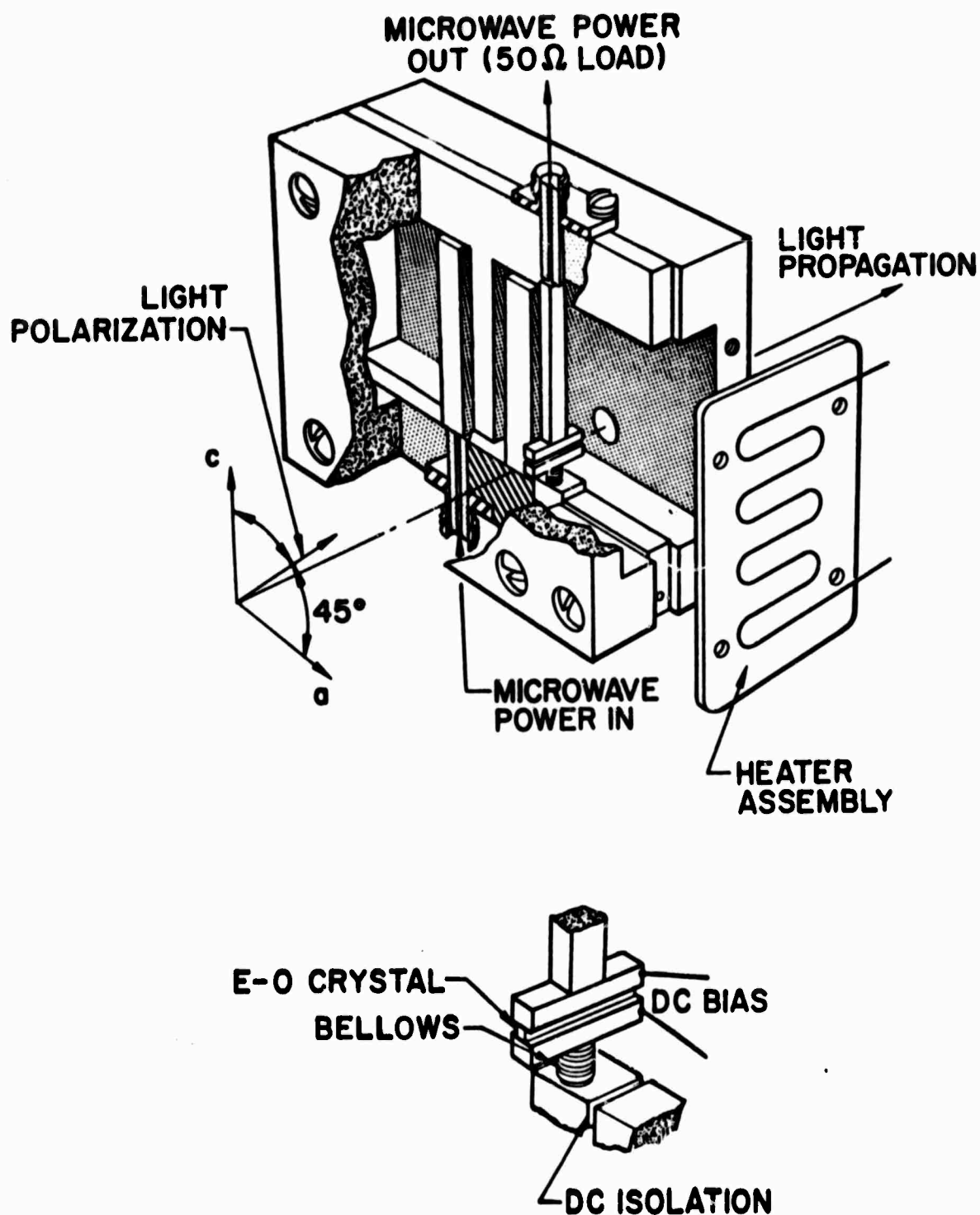


**Fig. 1-1 1- to 2-GHz Modulator, Showing Details of Electrooptic Crystal Assembly for Automatic Electrooptical Bias**

One approach that is being pursued is the investigation of rf filter designs having internal or terminal impedance characteristics different from conventional designs so that, for a given rf power-flow through the circuit, high rf voltage across the modulating crystal may be obtained. Unfortunately, conventional filter theory has been concerned primarily with terminal characteristics rather than internal characteristics. Therefore, if the internal characteristics were to be varied as independent design parameters, new theoretical formulations had to be developed. We have found that only a moderate change in conventional theory is required to achieve a design suitable for our purpose if the terminal characteristics are allowed to vary. A detailed discussion with our consultant, Professor George Matthaei, has aided us in the theoretical reformulation. Basically, this approach allows the attenuation characteristics within the pass band to be relaxed slightly so as to give more flexibility to the output-section design necessary to arrive at the desired higher rf voltage per unit power-flow. Design efforts have been concentrated on this approach. A computer program has been set up and preliminary design results are now under examination.

Another approach to improving modulator efficiency is to use an interferometric mode of operation rather than the usual birefringence mode, the latter of which requires a polarizer to obtain intensity modulation. In the interferometric mode, the crystal, driven in the same interdigital filter structure, is part of a high-transmission Fabry-Perot etalon. Theoretical studies have indicated that increased efficiency is possible using this mode of operation. However, for the interferometric mode, the optical bias point is determined by the optical length of the crystal and cannot be controlled by an external Babinet compensator as in the case of the birefringence mode. Therefore, a controller device must be used; such a device is also useful for birefringence modulation. During the first quarter, uncoated  $\text{LiNbO}_3$  crystals which had a reflectivity of 14% were tested. The results showed good agreement with theory. During the second quarter,  $\text{LiNbO}_3$  crystals of 30-35% end reflectivities were obtained for this use; such reflectivities represent the practical optimum for the currently obtainable crystals. A controller device was designed and fabricated for automatically adjusting optical bias. Test results showed that automatic stabilization of the optical bias over a long period by means of electrooptic/thermal compensation was achieved.

Studies of more efficient electrooptic crystals for the modulator constitute another important approach. Samples of barium sodium niobate and strontium barium niobate have been obtained from crystal growers. Static birefringence tests and preliminary modulation tests have indicated that the optical quality of these materials is questionable. Nevertheless, because they are the only materials currently available, additional tests have been planned. These crystals are being antireflection (AR) coated for both 1.06- and 0.53- $\mu\text{m}$  wavelengths; and more careful measurements are scheduled.

The problems of crystal optical damage and stability in vacuum also have been carefully examined. It was found that no optically induced damage occurred in  $\text{LiNbO}_3$  when it was maintained at 170°–180°C at optical power densities of 14  $\text{kW}/\text{cm}^2$  (0.4880- and 0.5145- $\mu\text{m}$  radiation). Also, no measurable beam deviation from Gaussian was observed at these densities. The stability of  $\text{LiNbO}_3$  in vacuum was good: no discoloration occurred. One sample of  $\text{Sr}_{0.6}\text{Ba}_{0.4}(\text{NbO}_3)_2$  was found to discolor slightly at an optical intensity of 9  $\text{kW}/\text{cm}^2$ . However, not enough data are yet available to determine whether this discoloration is an intrinsic property of SBN.

In the remaining period, the theoretical design for the interdigital modulator will be further refined and prototypes will be built. Additional measurements of interferometric modulation using the 30–35% reflectivity  $\text{LiNbO}_3$  crystals will be made. The more efficient  $\text{Ba}_2\text{Na}(\text{NbO}_3)_5$  and  $\text{Sr}_{0.5}\text{Ba}_{0.5}(\text{NbO}_3)_2$  crystals will be AR coated and tested for birefringence modulation. Additional refinement of the automatic control circuit will also be pursued to arrive at a versatile laboratory tool for the measurement of both birefringence and interferometric modulation.

### 1.3 LIST OF PUBLICATIONS

The following is a list of publications of work that has been supported in part by this contract.

- (1) P. S. Castro, K. K. Chow, H. V. Hance, W. B. Leonard, R. C. Ohlmann, S. E. Patterson, D. G. Peterson, R. B. Ward, and R. F. Whitmer, "A 1-Gbit/sec CW Laser Communication Experiment," Paper 13-B.8, IEEE/OSA Conference on Laser Engineering and Applications, Washington, D.C., 2–4 Jun 1971

- (2) W. Culshaw and J. Kannelaud, "Two-Component Mode Filters for Optimum Single-Frequency Operation of Nd:YAG Lasers," IEEE JQE, Aug 1971
- (3) H. V. Hance, K. K. Chow, R. C. Ohlmann, D. G. Peterson, and R. B. Ward, "Modulation/Demodulation Techniques for an Optical 1-Gigabit/Second Inter-satellite Data Transmission System," to be presented at International Telemetry Conference, Washington, D.C., 27-29 Sep 1971



## Section 2

### SINGLE-FREQUENCY Nd:YAG STUDIES

#### 2.1 INTRODUCTION

The basic designs of low-loss intracavity mode filters developed for the single-frequency operation of Nd:YAG lasers were discussed in the First Quarterly Report. The more adequate mode filtering obtained with two-component mode filters, such as an intracavity tilted Fabry-Perot etalon and a metallic film, or a double metallic film etalon, has been further established, both theoretically and experimentally. The problem of single-frequency operation of the Nd:YAG laser at the 1-W level of output is basically solved, and it is now a question of determining optimum practical designs which embody efficiency, simplicity, and reliability, together with adequate mode selectivity. Studies were made on tilted intracavity Fabry-Perot etalons having high enough reflectivity for the suppression of adjacent axial modes at all nominal levels of laser gain, and with wide, free spectral ranges. The insertion loss of such highly reflective tilted etalons, including the so-called coating loss, must be experimentally determined, since if these losses are not excessive, thin 75 to 85% reflective etalons will be satisfactory for some applications.

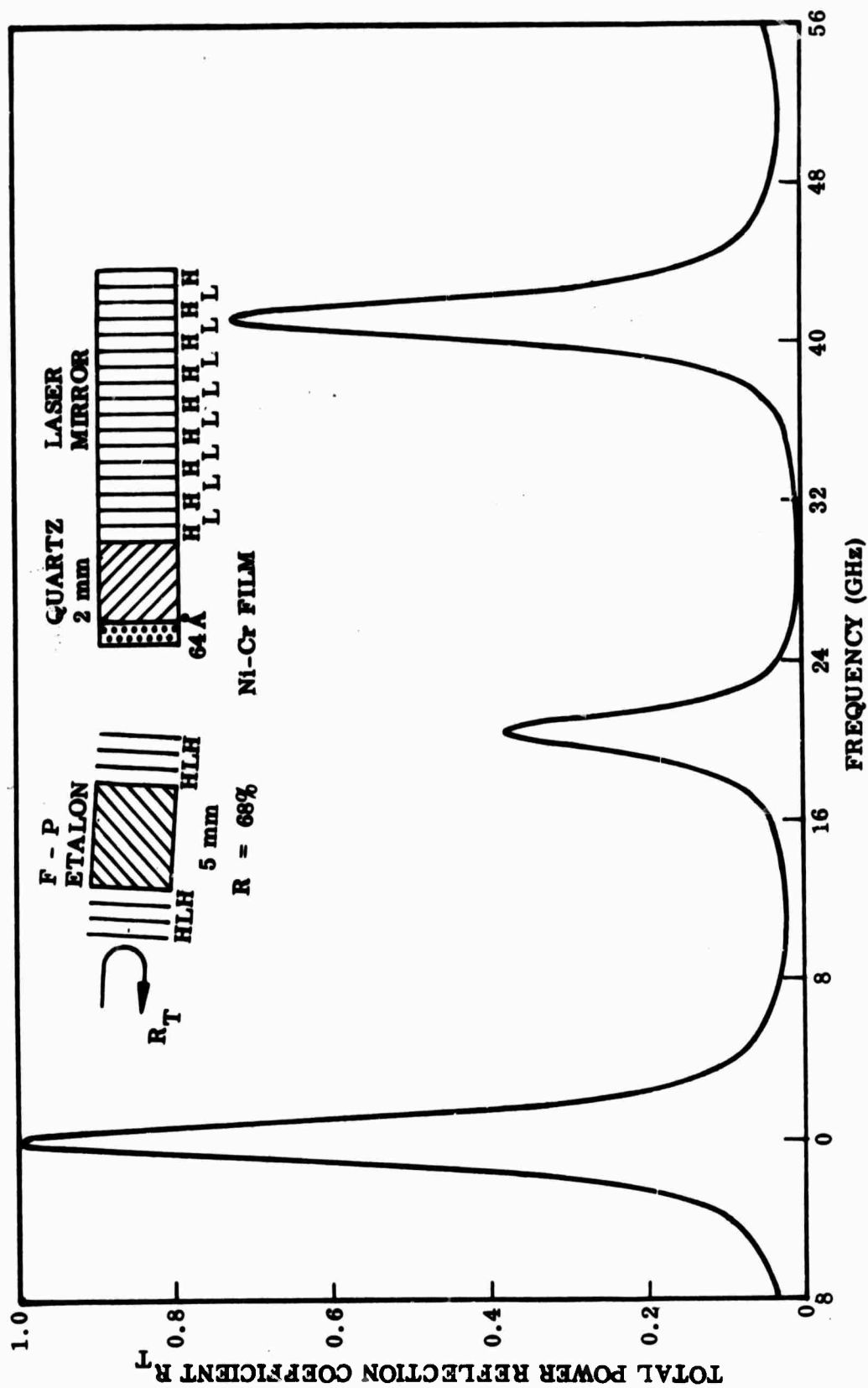
The two-component tilted Fabry-Perot etalon-metallic film combination is a very practical device that will guarantee single-frequency operation at the 1-W level of output power. Work on this mode selector is presently directed toward optimum component design and further experimental confirmation of its performance. Additional work was also done on the double-metallic-film mode filter, with encouraging results for single-frequency operation. This is a more sensitive mode filter, which requires good laser stability. Its chief advantage is that of a potentially lower insertion loss than any other mode filter devised to date.

One basic problem is that of accurate measurements of the intracavity losses introduced by the various mode filters. The development of a 1-W Nd:YAG operating at 100 to 150W of input power requires a more efficient high-pressure potassium lamp or semiconductor diode pump source, but it also requires laser operation with absolutely minimal intracavity loss. Some work on these problems has been done. The tilt loss of intracavity Fabry-Perot etalons has been computed for various cavity modes, waist sizes, etalon thickness and reflectivity, etc., by a more accurate method than heretofore employed, using the concept of an angular spectrum of plane waves that constitutes the particular cavity mode under consideration. A good basis for comparison of the tilt losses of various etalons and cavity modes has thus been established. The theory also indicates the potential use of Fabry-Perot etalons as transverse mode filters, thereby possibly obviating the need for critical intracavity apertures to obtain the TEM<sub>00</sub> mode of operation.

A design for a laser output mirror having a continuously variable power transmission coefficient has been evolved and is being fabricated. This will permit accurate comparison of the insertion losses of the various mode filters and also of the measurement of laser gain, insertion loss, and threshold in a direct and continuously variable manner. A high-pressure potassium lamp was also obtained during the last quarter, and work was initiated to determine its pumping efficiency in appropriate laser and pump cavity designs.

## 2.2 TILTED FABRY-PEROT ETALON AND METALLIC FILM MODE SELECTOR

Preliminary results on the single-frequency operation of the Nd:YAG laser with this two-component mode filter were given in the last report. During the last quarter, attention was given to more optimum designs of this two-component mode filter with reference to the free spectral ranges of the components, and the facility of single-frequency operation of the laser. Such single-frequency operation is now obtained on a routine basis within our laboratory. Figures 2-1a and 2-1b show the overall power reflection coefficients of this two-component mode filter for the two configurations



(a) Frequency Response for 5-mm, 68% Reflective Quartz F-P Etalon and 2-mm, 64 Å Nichrome Film-Laser Mirror Quartz Etalon

Fig. 2-1 Tilted Fabry-Perot Etalon - Nichrome Film Mode Filter for Single-Frequency Nd:YAG Lasers. Total power reflection coefficient versus frequency deviation from resonance condition



that are being studied. The desired operating laser frequency corresponds to zero on the frequency scale, where the power reflection coefficient of the composite mode filter is close to unity. The selectivity of the Fabry-Perot etalon then provides a sufficient reduction in the power reflection coefficient to eliminate adjacent axial or longitudinal modes of the particular laser resonator, while the possibility of additional laser oscillations at other free spectral ranges of the Fabry-Perot etalon is eliminated by the falloff in the power reflection coefficient due to the thin ( $64\text{\AA}$ ) nichrome film - laser mirror etalon.

The longer tilted Fabry-Perot etalon of lower reflectivity is the best arrangement, since its insertion loss is smaller. This is particularly true if the coating losses of the etalons become more serious at the higher reflectivities, a factor that is under investigation. However, it is apparent from Figs. 2-1a and 2-1b that the combination is an excellent practical solution to the mode selection problem in the Nd:YAG laser. The final choice of parameters will depend on measurements of the respective insertion losses, as outlined later in the report. Such losses can be made quite small using the appropriate filter combination. Single-frequency operation of the Nd:YAG laser at the 1-W output level should be obtained with this arrangement, which is quite practical and not unduly difficult to implement.

### 2.3 TILT LOSS OF INTRACAVITY FABRY-PEROT ETALONS AND TRANSVERSE MODE CONTROL

Since the intracavity Fabry-Perot etalon is very suitable for single-frequency lasers and for mode control, it is important to derive expressions for its insertion losses. In general, the etalon is tilted to decouple it effectively from the laser mirror adjacent to the waist, where the etalon is situated. Various intracavity losses are introduced by such etalons, and approximate expressions for the so-called tilt loss have previously been deduced from the walkoff of the laser beam in the etalon. However, such etalons effectively act as plane wave filters, passing waves with propagation constants approximating the resonance condition. It is therefore more appropriate to deduce the tilt loss from considerations involving the incident angular spectrum of plane waves

corresponding to the given modal distribution of the electric field in the cavity. It follows that losses occur even at normal incidence, depending on the etalon parameters, laser beam mode, and waist size.

Referring to Fig. 2-2, the electric field and its associated angular spectrum may be written as

$$E_x(x, z) = \int B(k_x) e^{i(k_x x + k_z z)} dk_x \quad (2.1)$$

$$B(k_x) = (2\pi)^{-1} e^{-ik_z z} \int E_x(x, z) e^{-ik_x x} dx$$

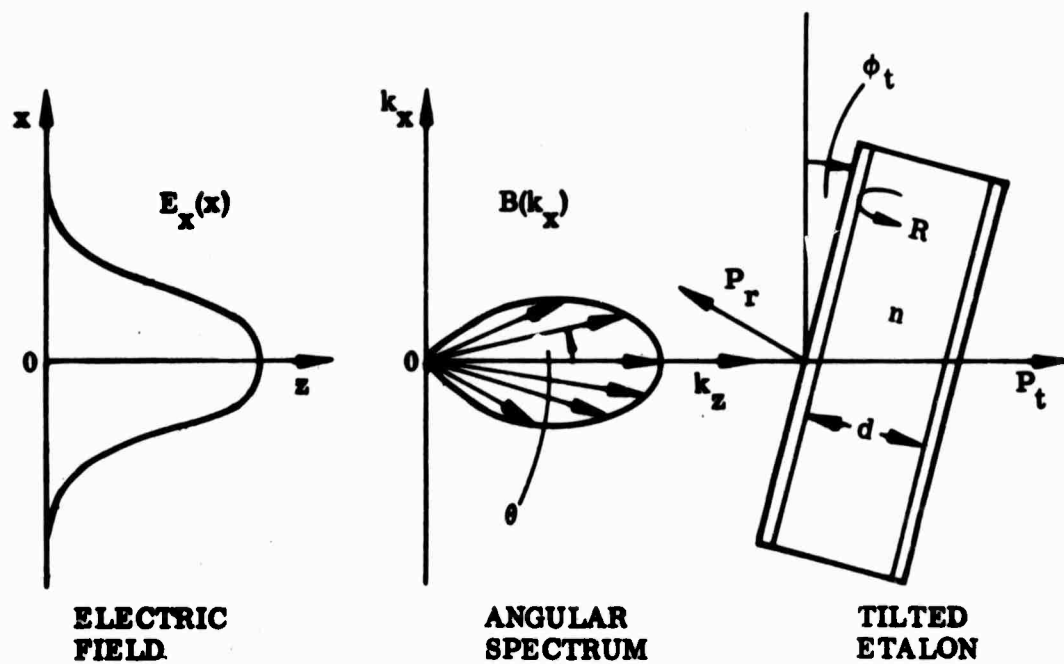
for the two-dimensional case, where  $k_x$  and  $k_z$  are the components of the wave vector  $\underline{k}$ . For example, at  $z = 0$ , which is the waist position, the electric field of the  $TEM_{00}$  mode and its angular spectrum are given by

$$E_x(x) = e^{-x^2/a^2} \quad (2.2)$$

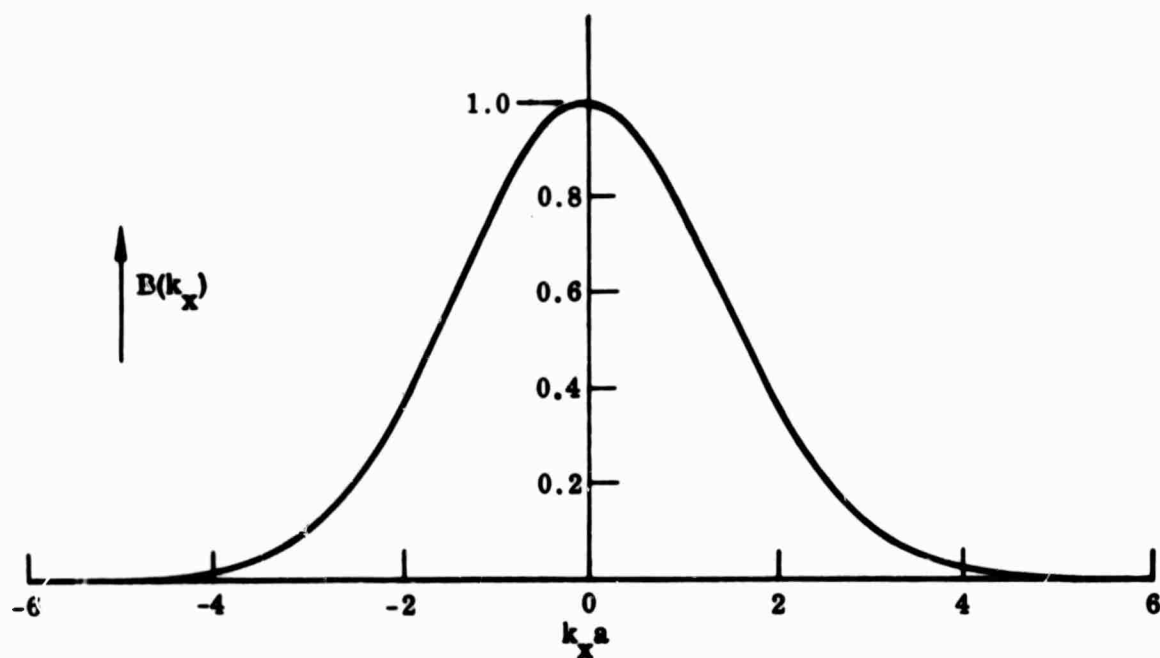
$$B(k_x) = (2\sqrt{\pi})^{-1} a e^{-k_x^2 a^2/4}$$

where  $a$  is the waist size. Similarly, the angular spectra of other transverse modes may be deduced from Eq. (2.1) using the known electric field distributions.

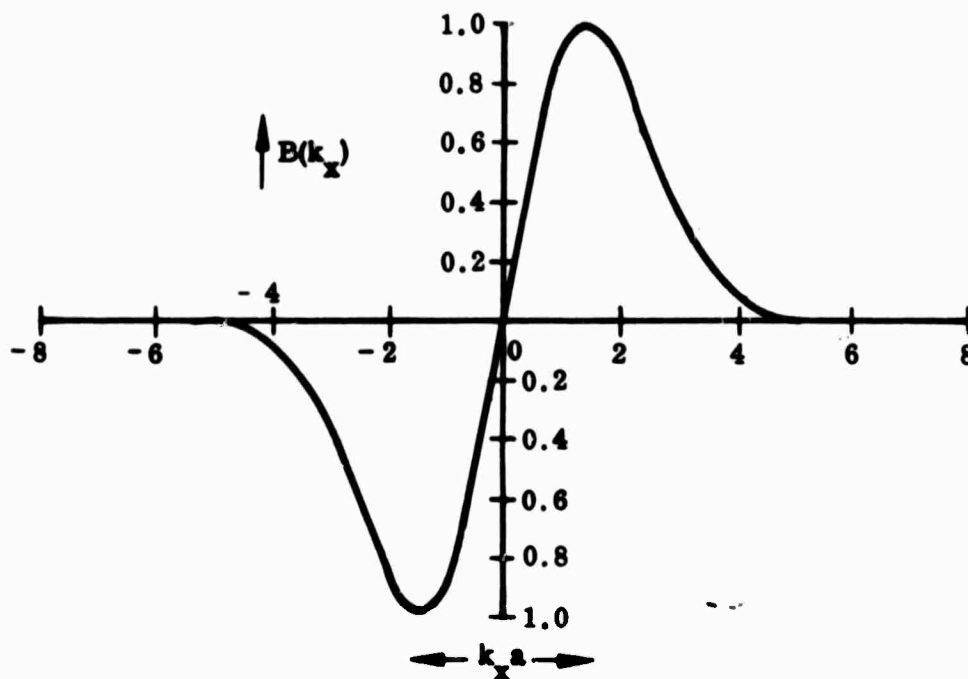
Figures 2-3a through 2-3h show such angular spectra computed for Gaussian beam modes  $TEM_{00}$  through  $TEM_{70}$ . The abscissa  $k_x a$  makes the curves apply for all waist sizes, and by replacing this with  $2x/a$  the same curves give the electric field distributions of the modes apart from some unimportant phase reversals. It is clear that the higher transverse modes lead to a wider angular spectrum of plane waves, and an appropriate intracavity Fabry-Perot etalon may be designed to eliminate such oscillating modes. The suppression of the  $TEM_{10}$  mode will be more difficult without



**Fig. 2-2 Distribution of the x-Component of the Electric Field Along the x-Axis; the Corresponding Angular Spectrum of Plane Waves; and the Parameters of the Tilted Fabry-Perot Etalon**



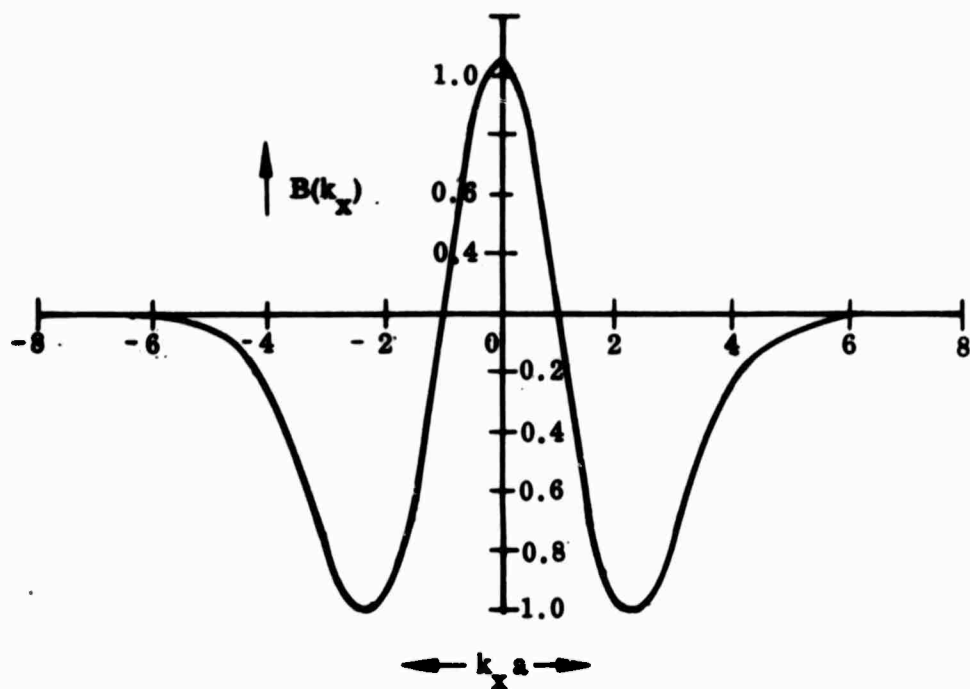
(a)  $TEM_{00}$  Mode,  $B(k_x) \propto \exp [-(k_x a)^2/4]$



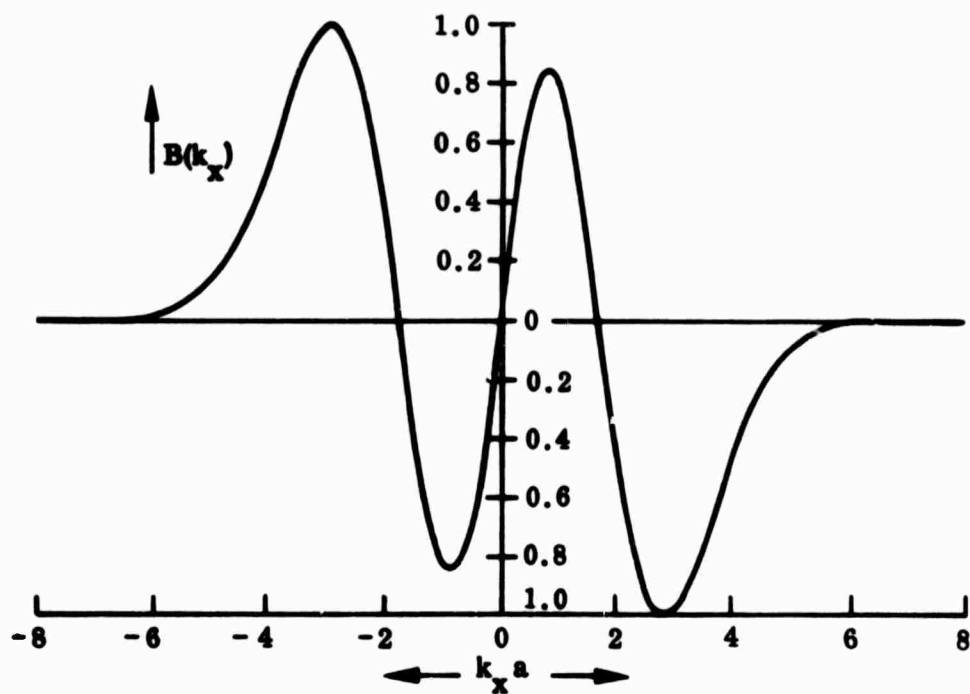
(b)  $TEM_{10}$  Mode,  $B(k_x) \propto k_x a \exp [-(k_x a)^2/4]$

Fig. 2-3 Angular Plane Wave Spectra of Gaussian Beam Laser Resonator Modes,  $B(k_x)$  Versus  $k_x a$ , Where  $k_x$  Is the x-Component of the Plane Wave Propagation Constant and  $a$  Is the Beam Waist



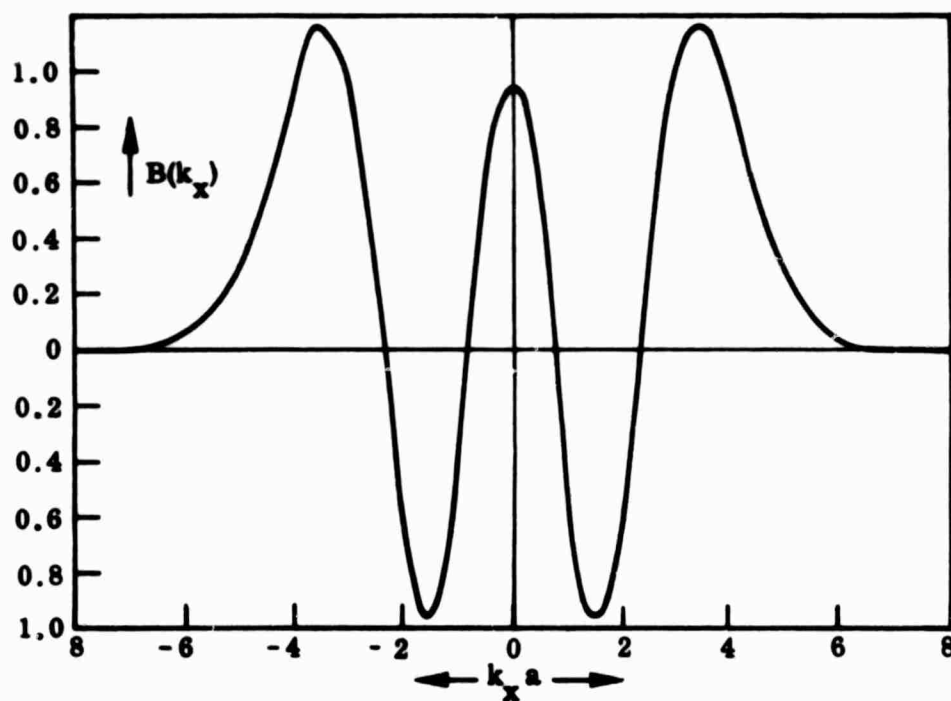


(c) TEM<sub>20</sub> Mode,  $B(k_x) \propto (1 - k_x^2 a^2) \exp [-(k_x a)^2/4]$

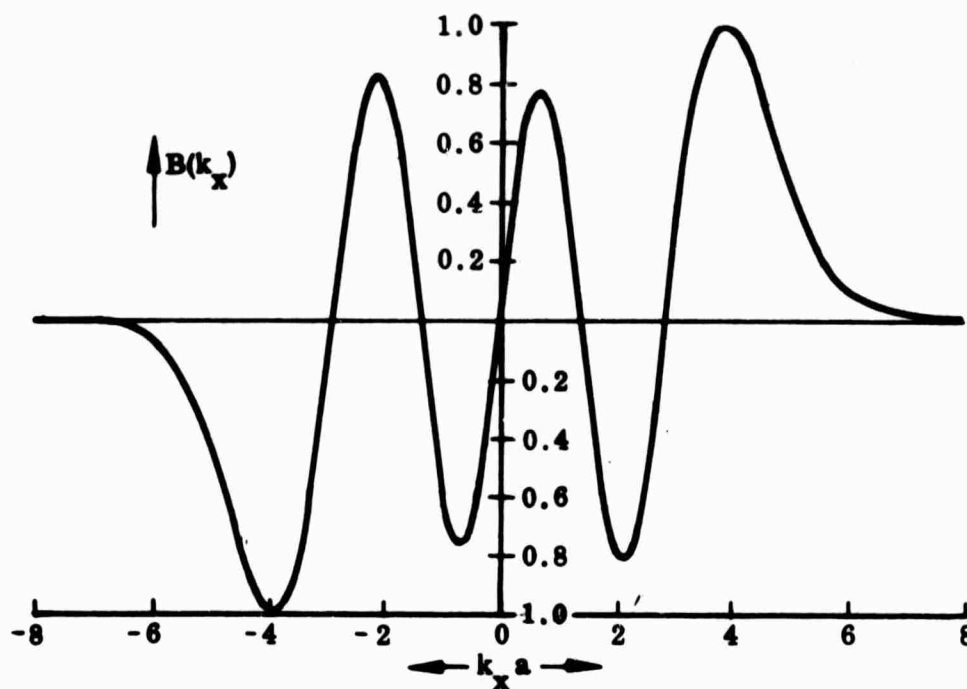


(d) TEM<sub>30</sub> Mode,  $B(k_x) \propto [3 k_x a - (k_x a)^3] \times \exp [-(k_x a)^2/4]$

Fig. 2-3 (Cont.)

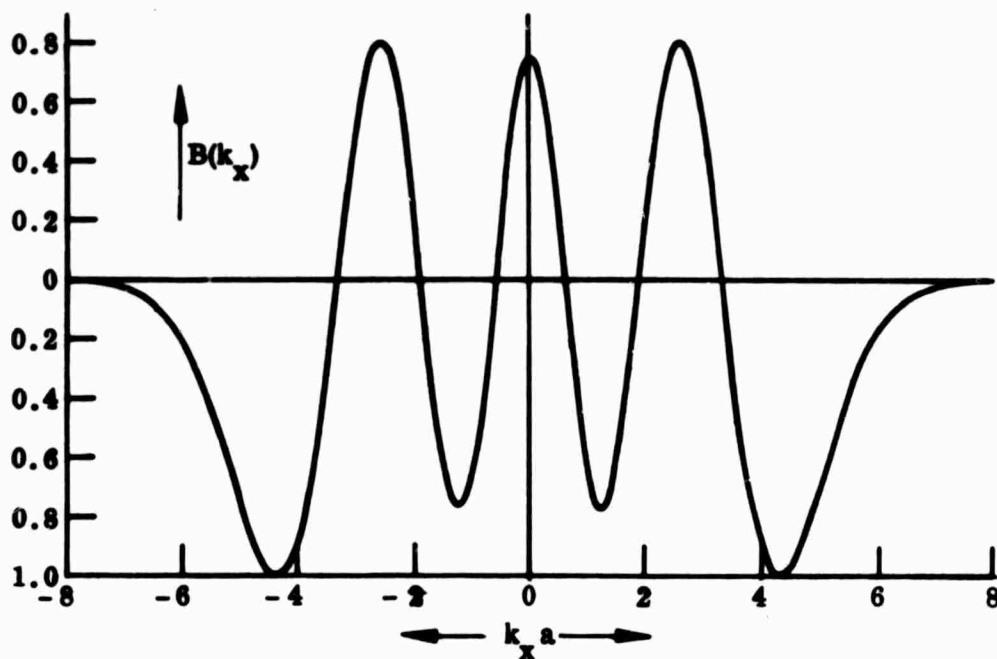


(e) TEM<sub>40</sub> Mode,  $B(k_x) \propto [(k_x a)^4 - 6(k_x a)^2 + 3] \times \exp[-(k_x a)^2/4]$

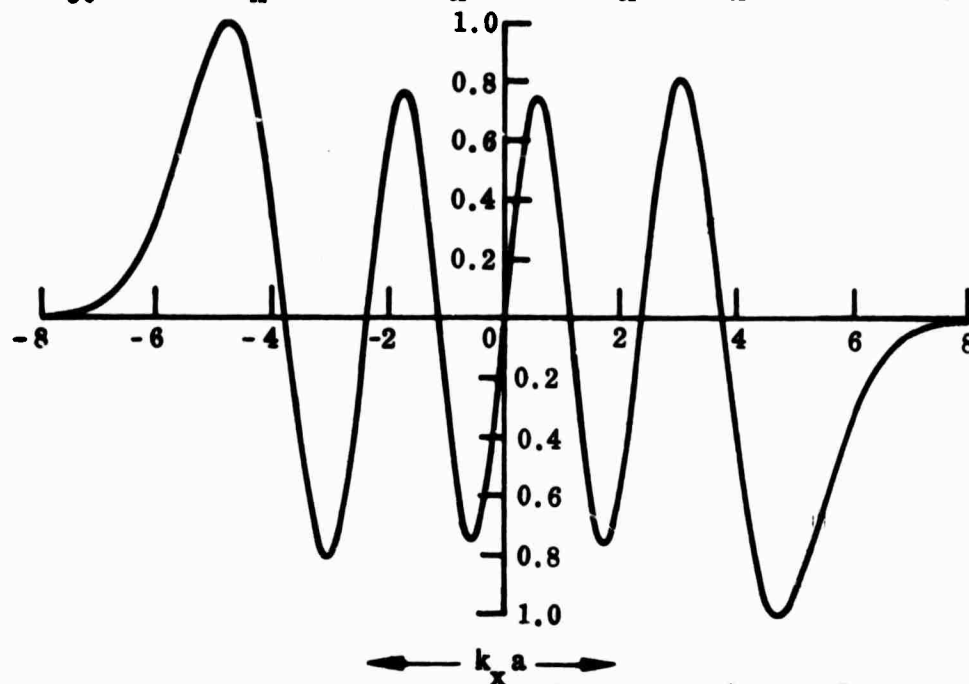


(f) TEM<sub>50</sub> Mode,  $B(k_x) \propto [(k_x a)^5 - 10(k_x a)^3 + 15 k_x a] \exp[-(k_x a)^2/4]$

Fig. 2-3 (Cont.)



(g) TEM<sub>60</sub> Mode,  $B(k_x) \propto [15 - 45(k_x a)^2 + 15(k_x a)^4 - (k_x a)^6] \exp[-(k_x a)^2/4]$



(h) TEM<sub>70</sub> Mode,  $B(k_x) \propto [105 k_x a - 105(k_x a)^3 + 21(k_x a)^5 - (k_x a)^7] \exp[-(k_x a)^2/4]$

Fig. 2-3 (Cont.)

introducing some insertion loss for the  $TEM_{00}$  mode. However, this is probably no more serious than using an intracavity iris for this purpose, and in contrast the etalon requires no precise axial alignment.

The power reflection and transmission coefficients of the tilted etalon have been deduced and are given by

$$P_r = \pi \eta_0 \int \frac{|B(k_x)|^2 4R \sin^2 \left[ (k'_z + k_z) d / (2 \cos \phi_t) \right]}{1 - 2R \cos \left[ (k'_z + k_z) d / \cos \phi_t \right] + R^2} dk_x$$

and

$$P_t = \pi \eta_0 \int \frac{|B(k_x)|^2 (1 - R)^2}{1 - 2R \cos \left[ (k'_z + k_z) d / \cos \phi_t \right] + R^2} dk_x \quad (2.3)$$

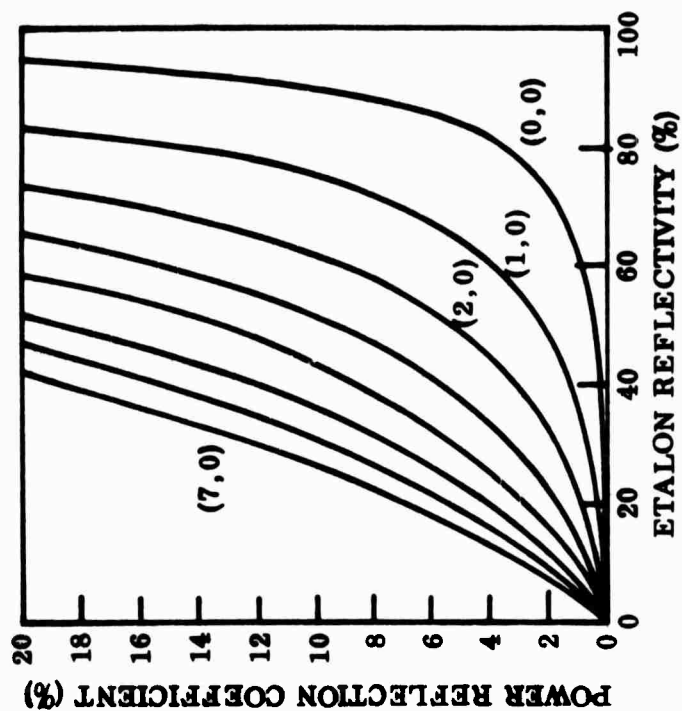
respectively, where  $\eta_0$  is the admittance of free space,

$$k'_z = k_z \cos(2\phi_t) - k_x \sin(2\phi_t)$$

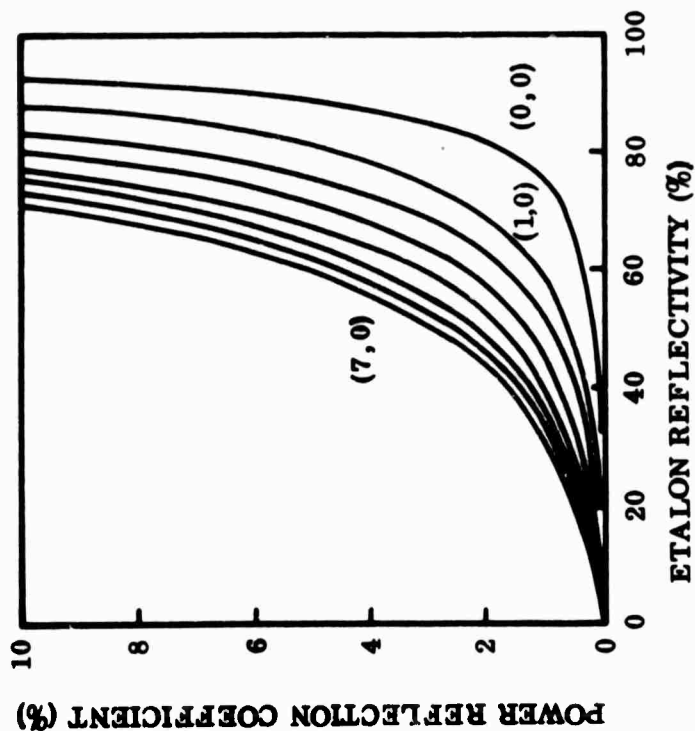
$$k_z = (k^2 n^2 - k_x^2)^{1/2}$$

$n$  is the refractive index of the etalon,  $R$  is its reflectivity, and  $\phi_t$  is the tilt angle as shown in Fig. 2-2. Values of  $P_r$  and  $P_t$ , normalized to  $R = 0$ , have been computed from Eq. (2.3) as functions of the etalon parameters (reflectivity or selectivity, thickness, refractive index, and tilt angle) for various waist sizes and modes of the resonator.

Figure 2-4a shows the percentage reflection coefficient, or loss, of a 1-cm-thick quartz etalon as a function of its reflectivity  $R$  for a waist size of 0.02 cm and a tilt-angle of zero degrees or normal incidence. Curves are shown for the  $TEM_{00}$  through  $TEM_{70}$  cavity modes. It is apparent that a considerable degree of higher transverse mode rejection can be obtained with such intracavity etalons. Figure 2-4b shows a similar



(a) Etalon Reflectivity. Etalon thickness, 1 cm; refractive index, 1.5; beam waist, 0.02 cm; tilt angle, 3 arcmin



(b) Etalon Reflectivity. Etalon thickness, 1 cm; refractive index, 1.5; beam waist, 0.06 cm; tilt angle, 3 arcmin

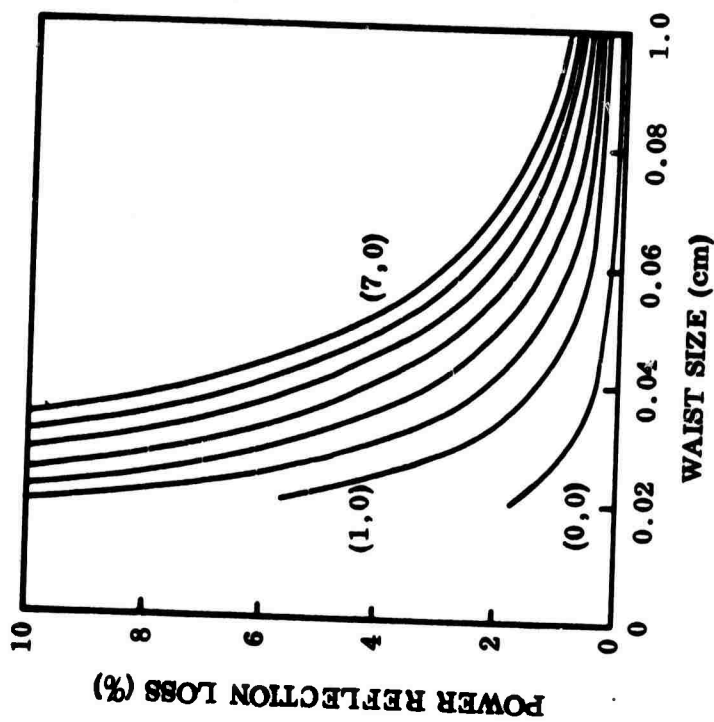
Fig. 2-4 Power Reflection Coefficients or Power Loss of the Tilted Fabry-Perot Etalon Versus Design Parameters for Laser Resonator Modes TEM<sub>00</sub> Through TEM<sub>70</sub>

curves for a waist size of 0.06 cm and a tilt-angle of 3 min of arc, when the reflection loss is reduced due to the larger waist size. Figure 2-4c shows curves of reflection loss versus waist size for a 60% reflective quartz etalon 1 cm thick and a tilt angle of 3 min. The rapid decrease in reflection loss with waist size for all modes is apparent from these curves. Figure 2-4d shows curves of reflection loss versus quartz etalon thickness for a 60% reflective etalon and a waist size of 0.06 cm. Figure 2-4e shows the increase in reflection loss versus tilt angle for a 1-cm-thick quartz etalon of 60% reflectivity and a waist size of 0.06 cm.

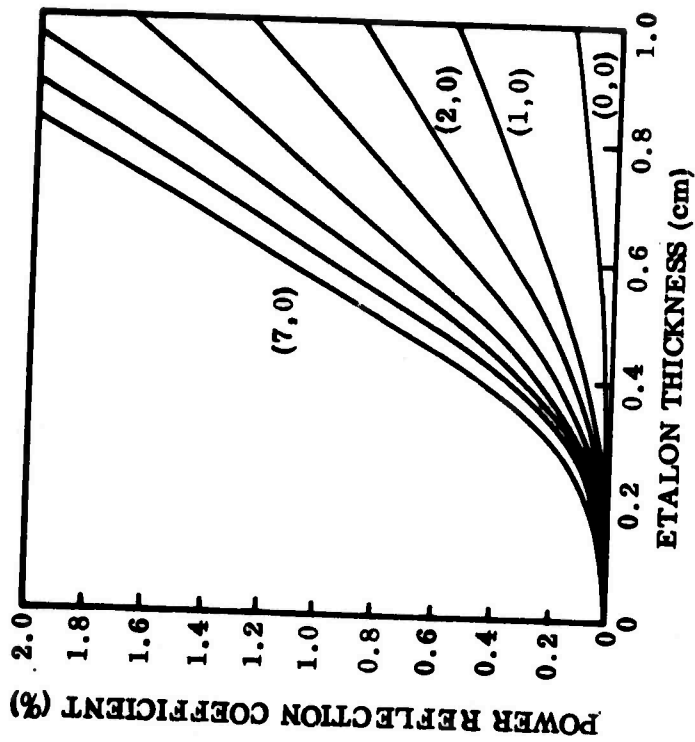
Using these results, optimum designs of intracavity Fabry-Perot etalons may be developed both for single-frequency operation of Nd:YAG lasers and for the rejection of transverse modes of the cavity. The concept of an angular spectrum of plane waves corresponding to the modal distribution of the electric field is very useful. In fact, the complete expressions for the propagation of Gaussian beams, i.e., beam waist expansion, phase variation, and wave front curvature, may be deduced directly from the propagation of such modal plane wave angular spectra. An optical cavity consists of mirrors at the appropriate distances and of curvature such that the composite angular spectrum is reflected back and forth in the usual manner.

#### 2.4 DOUBLE METALLIC FILM MODE SELECTOR

Figures 2-5a and 2-5b show computed curves of the reflectivity of a 2-mm-thick quartz etalon coated with 64Å nichrome films and placed at distances of 2.2 and 1.1 cm, respectively, from the laser mirror. A comparison of these curves with those of the tilted etalon - metallic film mode filter in Figs. 2-1a and 2-1b shows the advantages of the latter type. The numerous resonances in the double metallic film etalon arise from the lower free spectral range of the etalon-mirror distance. Practical considerations currently limit this to a few centimeters, although in any event it must be large enough to reduce the overall reflectivity sufficiently to prevent oscillations in adjacent axial modes of the laser resonator. Also the precise positioning and good laser stability required for this mode filter make it less suitable as a practical mode filter for the single-frequency operation of the Nd:YAG laser.

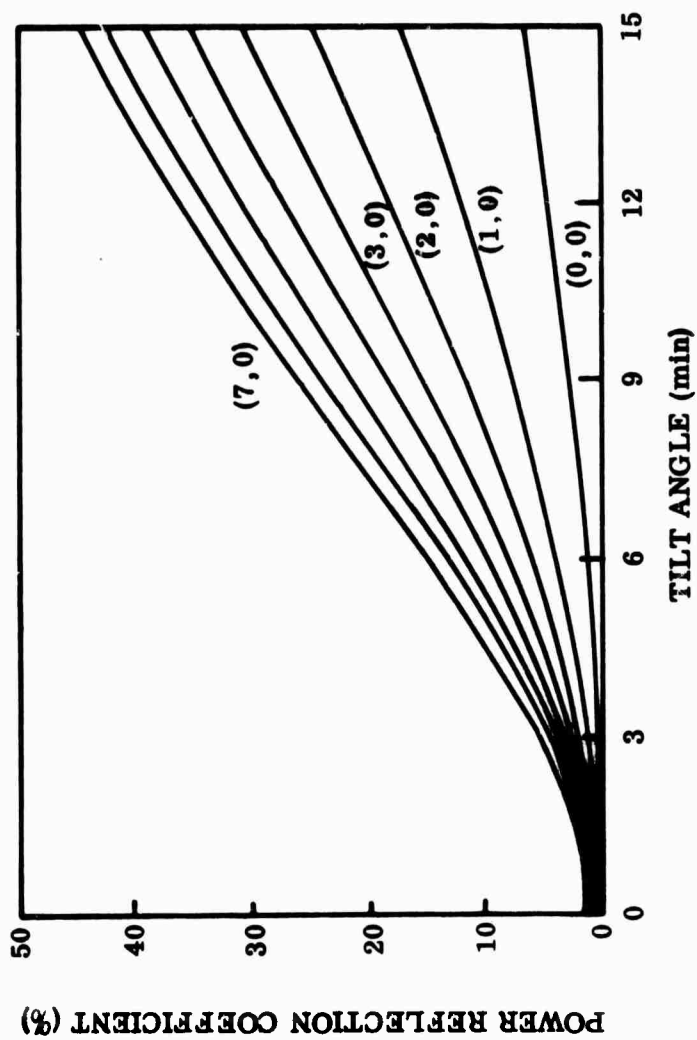


(c) Waist Size (in centimeters). Etalon thickness, 1 cm; etalon reflectivity, 50%; refractive index, 1.5; tilt angle, 3 arcmin



(d) Etalon Thickness (in centimeters). Beam waist, 0.06 cm; etalon reflectivity, 50%; refractive index, 1.5; tilt angle, 3 arcmin

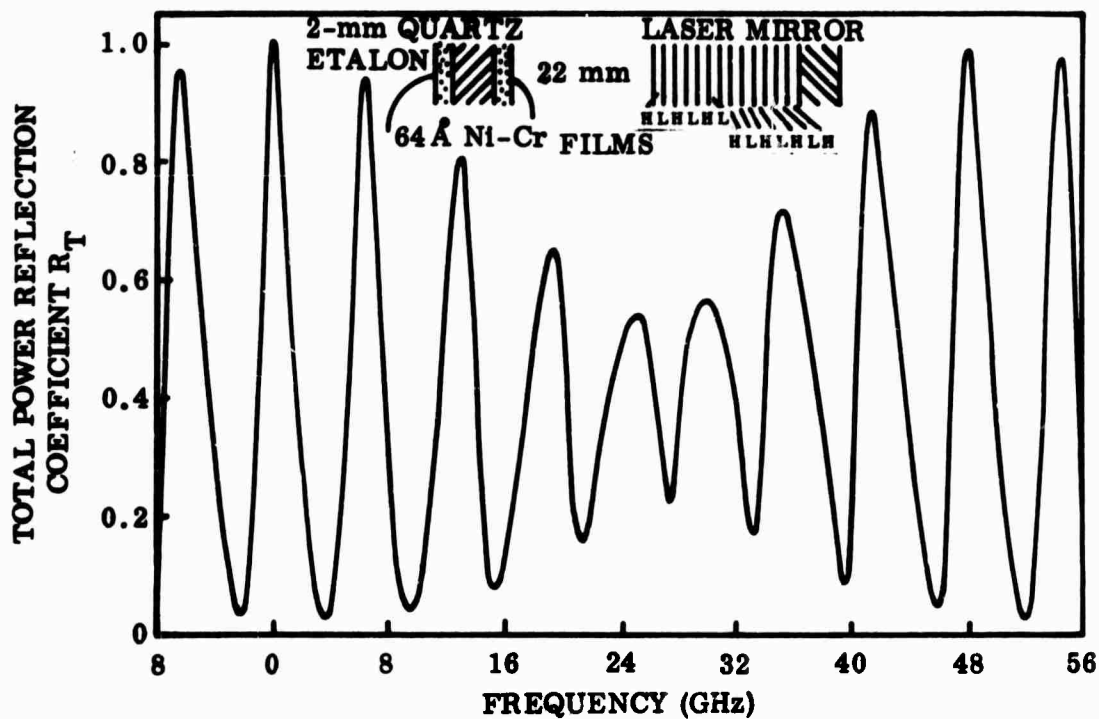
Fig. 2-4 (Cont.)



(e) Tilt Angle (in minutes). Beam waist, 0.06 cm; etalon thickness, 1 cm; etalon reflectivity, 60%; refractive index, 1.5

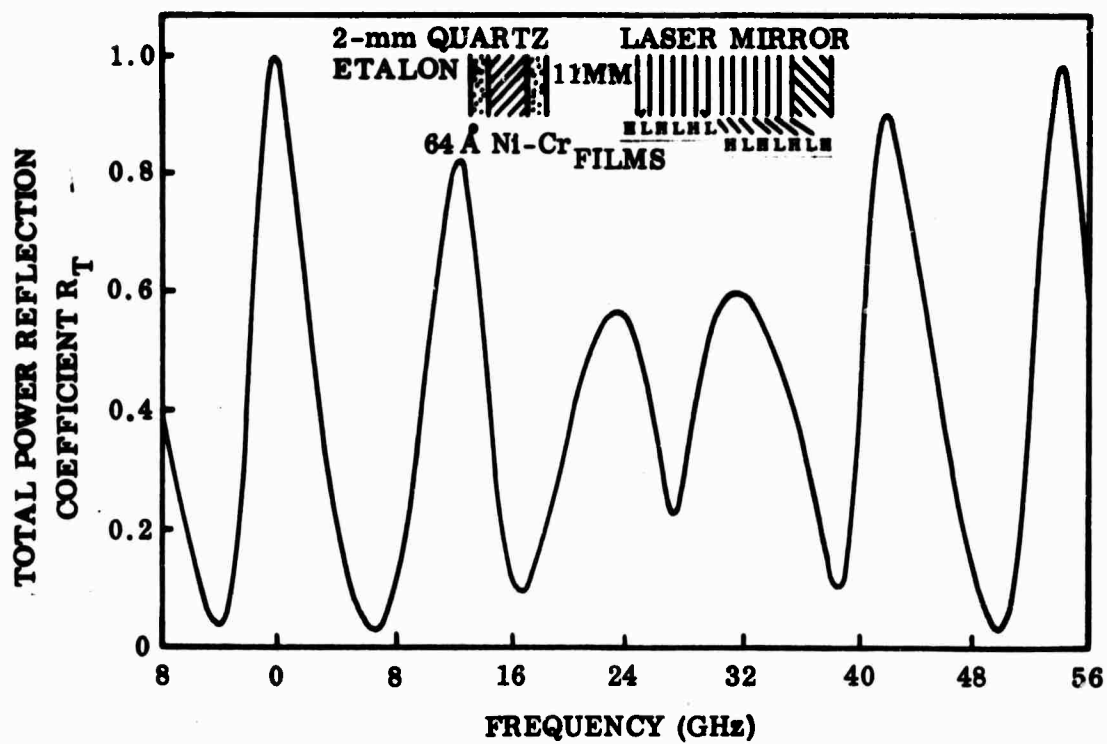
Fig. 2-4 (Cont.)





(a) Frequency Response for 64 Å Nichrome Films on a 2-mm Quartz Etalon Spaced at 2.2 cm From the Laser Mirror

Fig. 2-5 Double-Nichrome-Film Quartz Etalon Mode Filter for Single-Frequency Nd:YAG Lasers; Total Power Reflection Coefficient Versus Frequency Deviation From Resonance Condition



(b) Frequency Response for 64 Å Nichrome Films on a 2-mm Quartz Etalon Spaced at 1.1 cm From the Laser Mirror

Fig. 2-5 (Cont.)

During the first quarter, a double metallic film mode selector with 42-Å-thick nichrome films on a 5-mm-thick quartz etalon was tested in the Nd:YAG laser. The closest spacing between the end reflector and the metal film possible in our present laser was 4 cm; and this, together with the 42Å film thickness, did not provide sufficient selectivity against frequencies spaced at other free spectral range spacings to enable single-frequency operation at the full kilowatt level of pump power. As expected, the 4-cm distance between the nichrome film and the laser mirror gave excellent discrimination against adjacent axial modes. However, because of the free spectral range limitations and nichrome film thicknesses used, oscillations did, in general, occur at more than one frequency. Depending on the reflector-etalon spacing, observed frequencies were about 4 GHz or 20 GHz apart, corresponding to the free spectral ranges of the etalon-reflector distance and of the 5-mm quartz etalon, respectively. A more appropriate choice of these free spectral ranges and of nichrome film thickness could eliminate this difficulty in any future experiments, but, as discussed earlier, it may not be possible to eliminate such additional oscillations for all operating conditions of the Nd:YAG laser.

## 2.5 LASER MIRROR WITH VARIABLE TRANSMISSION COEFFICIENT

For the attainment of a single-frequency output at the 1-W level from a Nd:YAG laser with an efficiency of ~1%, it is mandatory that all cavity losses be reduced to an absolute minimum. The insertion loss of the various mode filters must be ascertained and designs optimized to make this minimal consistent with reliable single-frequency operation.

The steady-state behavior of a laser in which one mirror is 100% reflecting and the other has a power transmission coefficient  $T$  is described by the equation

$$\frac{2g_0}{1 + 2S P_c} = L_R + L + T \quad (2.4)$$

where  $g_0$  is the unsaturated single-pass gain,  $S$  is a saturation parameter,  $P_c$  is the one-way-circulating power in the laser cavity,  $L_R$  is the double-pass loss in the laser rod, and  $L$  is the double-pass loss in any other intracavity components. The power output of the laser is then given by  $P_o = T P_c$  and may be maximized with  $T$  as the only independent variable by selecting the optimum value of  $T$ . At threshold  $P_c = 0$ , and hence

$$2g_0 = L_R + L + T \quad (2.5)$$

The power output  $P_o$  is a maximum when

$$T_{opt} = \left[ 2g_0 (L_R + L) \right]^{1/2} - (L_R + L) \quad (2.6)$$

and the output power is then

$$P_o^{max} = (2S)^{-1} \left[ \sqrt{2g_0} - (L_R + L)^{1/2} \right]^2 \quad (2.7)$$

Figure 2-6 shows two designs of a laser output mirror having a variable transmission coefficient  $T$  which are being fabricated. Experimental curves of the output power  $P_o$  as a function of mirror transmission  $T$  may thus be obtained using the single-frequency laser whose frequency can be varied. From such results, together with Eqs. (2.5), (2.6), and (2.7), the laser parameters and the intracavity losses introduced by various mode filters may be determined in a reasonably direct way. This knowledge is essential to the development of efficient 1-W single-frequency Nd:YAG lasers.

## 2.6 FURTHER INVESTIGATIONS

During the next contract period, work will continue in the following areas:

- (1) Improvements in the thermal stability of the Nd:YAG rod and reduction of mechanical vibrations by improved designs of the rod holder to eliminate resonance and to obtain better alignment procedures

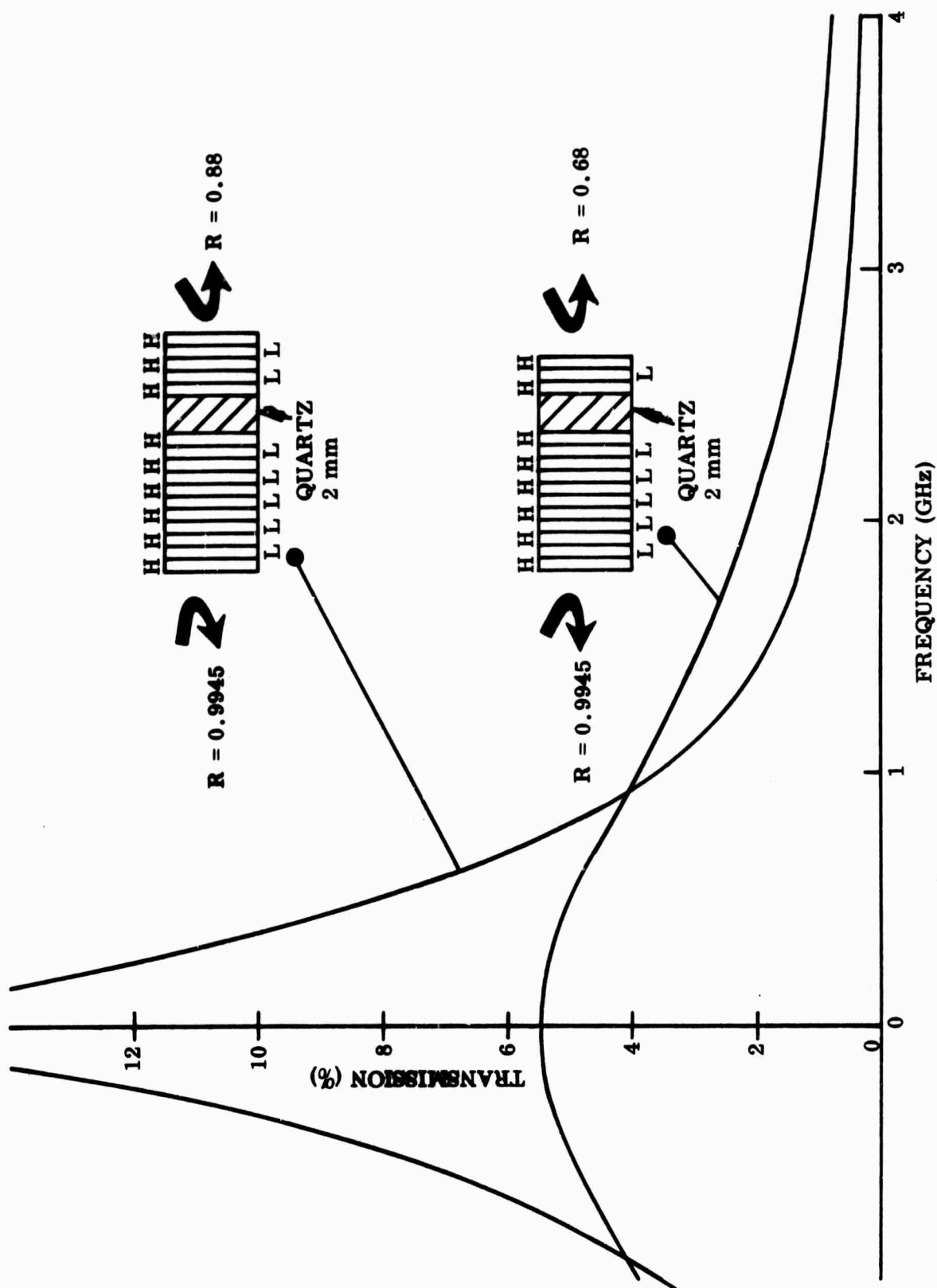


Fig. 2-6 Designs for a Laser Output Mirror With a Continuously Variable Power Transmission Coefficient for Gain, Loss, and Saturation Power Measurements on Operating Nd:YAG Lasers. The term  $R$  represents the separate reflectivities required on either side of the quartz substrate

- (2) Further tests on the use of thinner (2 mm) quartz Fabry-Perot etalons of higher reflectivity to evolve the simplest mode filter for single-frequency operation with 1 W of output power; also investigations of the use of 2-mm quartz double metallic film etalons for improved rejection of modes at other free spectral ranges
- (3) Further development and fabrication of laser output mirrors having continuously variable transmission coefficients, and studies of the intracavity losses of the various mode filters
- (4) Consideration of methods of stabilizing the single-frequency oscillation using frequency-selective intracavity etalons or external Fabry-Perot etalons in a feedback control loop
- (5) Development of cavity designs having internal focusing elements to obtain optimum  $TEM_{00}$  mode volumes in the Nd:YAG rod that match the pumping geometry and approach maximum efficiency
- (6) Use of such laser cavity designs with the present spherical pumping cavity and tungsten-iodine lamp to obtain output powers in excess of 0.5 W from the present single-frequency Nd:YAG laser
- (7) Investigations of use of the potassium-rubidium lamp for more efficient pumping of the Nd:YAG laser to obtain a single-frequency output of 1 W at high efficiency

### Section 3

#### WIDE-BANDWIDTH OPTICAL MODULATOR

In our efforts to improve the ultrawide-bandwidth optical modulator previously developed, work has proceeded on the theoretical analysis of the interdigital filter structure containing the electrooptic crystal, the theoretical and experimental tests on the interferometric mode of modulation, the design and construction of an automatic electrooptic/thermal controller for maintaining the optical bias of the modulator, and the evaluation of various crystals for use in the modulator. The basic modulator design has been demonstrated experimentally to have a modulation bandwidth of 1.2 GHz (0.9- to 1.2-GHz band) and a depth of modulation of 60% for 0.5145- $\mu\text{m}$  light with 5-W rf input. However, this basic modulator will give only about a 30% modulation depth at 1.06  $\mu\text{m}$  with 5-W rf drive, so that a means of increasing its efficiency must be pursued. These matters are being investigated under this contract, as mentioned.

#### 3.1 STUDY OF THE MODULATOR CIRCUIT

The modulator circuit is basically an interdigital bandpass filter having the electro-optic (EO) crystal at the output capacitance gap. The uniform electric field in this gap induces optical modulation on light focused through the crystal. Therefore, to increase the modulation index of the optical beam for a given rf drive power, the filter design must be so modified that either the internal or the terminating characteristics of the output section can be varied independently as design parameters in order to increase the rf voltage across the modulating crystal. Conventional filter design, however, is mainly concerned with terminal characteristics, not with internal characteristics. Therefore, to specify internal characteristics such as rf voltage, phase, impedance, etc., as design parameters necessitates a new theoretical approach starting from first principles. This was the approach considered during the first

quarter. On the other hand, if the terminating characteristics are allowed to vary so as to maximize the rf voltage across the crystal, subject to the requirements of bandwidth and attenuation ripple within the passband (PB), a useful design will also be obtainable. The latter approach utilizes most of the conventional design theory, requiring only a slight modification. Hence, with the imposed time limitation of this contract, the second approach appears to be more appropriate.

During the second quarter, these approaches were critically reexamined and the second approach was adopted. The problem has been formulated, and preliminary design results have been obtained, as will be discussed in the following paragraphs. For the sake of clarity and logical continuity, the discussion begins with the first principles of filter design, proceeds through the salient features of the derivation, and finally arrives at the preliminary design.

#### 3.1.1 Choice of Basic Filter Type

In general, there are two basic filter types: the Butterworth (maximally flat) and the Tchebyscheff (equal-ripple). The Tchebyscheff is generally favored by filter designers because of the sharp cutoff characteristics, although the Butterworth has a much more linear phase-delay characteristic. In our case, the Tchebyscheff design is still favored because of its circuit design versatility, which, as will be seen, is important for the modulator. Once the filter type is chosen, a low-pass prototype (LPPT) is usually selected as a starting point according to the desired attenuation characteristics with respect to frequency. The circuit elements of this LPPT are then determined by circuit synthesis techniques. After determination of the circuit elements, a transformation to the band of interest is performed. In fact, the attenuation characteristics and the values of normalized circuit elements for various LPPT's have been calculated and published in charts and tables (Refs. 1, 2).



### 3.1.2 Choice of the Low-Pass Prototype (LPPT) Filter

For the Tchebyscheff filter, the attenuation characteristics  $L_A(\omega')$  are given in decibels by

$$L_A(\omega') = 10 \log_{10} \left\{ 1 + \epsilon \cos^2 \left[ n \cos^{-1} \left( \frac{\omega'}{\omega'_1} \right) \right] \right\}_{\omega' \leq \omega'_1} \quad (3.1)$$

and

$$L_A(\omega') = 10 \log_{10} \left\{ 1 + \epsilon \cosh^2 \left[ n \cosh^{-1} \left( \frac{\omega'}{\omega'_1} \right) \right] \right\}_{\omega' \geq \omega'_1} \quad (3.2)$$

where

$$\epsilon = \left[ \text{antilog} \left( \frac{L_{Ar}}{10} \right) - 1 \right] \quad (3.3)$$

$n$  = number of reactive elements in LPPT circuit (number of poles)

$\omega'$  = low-pass frequency

$\omega'_1$  = low-pass band edge, i.e., maximum frequency at which  $L_A = L_{Ar}$

where  $L_{Ar}$  = maximum attenuation ripple, in decibels, within the PB

As can be seen from the equations, the attenuation ripple  $L_{Ar}$  and the cutoff characteristics  $L_A(\omega')|_{\omega' \geq \omega'_1}$  determine the number of poles for the LPPT. For a conventional filter design,  $L_{Ar}$  is usually kept as small as possible ( $L_{Ar} = 0.01$  dB is a typical value), since the maximum power transfer within the PB is of primary importance. For a modulator,  $L_{Ar}$  is not the primary concern, however, because the maximum rf E-field across the modulating crystal is the desired quantity.

(Obviously,  $L_{Ar}$  has to be kept within reasonable limits.) In addition, the cutoff characteristics are not important to the modulator, since the modulating signals are normally well confined in a given band through filtering processes during signal handling.

In the design of the modulator, therefore, one would vary the value of  $L_{Ar}$  within some limits to arrive at the circuit configuration that provides the desired rf voltage at the crystal. (This will be discussed in more detail in section 3.1.5.) This process also defines the number of reactances  $n$  in the LPPT circuit. The entire LPPT circuit, and consequently the cutoff characteristics outside the PB, are then completely specified. As mentioned earlier, once  $L_{Ar}$  and  $n$  are chosen, the circuit elements for a LPPT ladder network to realize such  $L_{Ar}$  characteristics can be obtained from tables.

As has been calculated (Ref. 1), for a given value of  $L_{Ar}$ , one reaches a state of diminishing returns in changing the circuit elements to achieve high rf voltage at the crystal when  $n > 4$ . On the other hand, one requires  $n \geq 4$  to achieve the required impedance transformation within the filter structure when the LPPT is transformed to the desired bandpass (BP) configuration. Therefore, for structural simplicity and high rf voltage at the EO crystal,  $n = 4$  is again chosen for the new modulator design. Upon transformation to the BP configuration, this results in four resonating inter-digits, as previously employed.

For a preliminary design,  $L_{Ar} = 0.5$  dB has been chosen. This corresponds to a theoretical maximum power transmission loss of 11%. In practice, a loss of 15% may be expected. This amount of loss (reflected toward the generator) is not considered significant enough to cause concern. However, the phase characteristics within the PB do deteriorate with increasing  $L_{Ar}$  and may eventually become a limiting factor in an actual communication system. With  $L_{Ar} = 0.5$  dB,  $n = 4$ , an LPPT ladder network is obtained, as shown in Fig. 3-1.

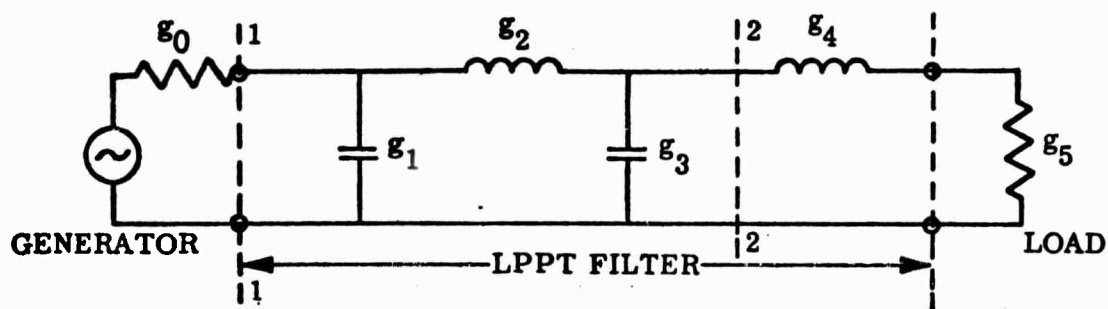


Fig. 3-1 A Low-Pass Prototype Tchebyscheff Filter Circuit, Normalized to  $\omega'_1 = 1$  rad/sec and Generator Impedance  $g_0 = 1\Omega$ . Values of  $g$ 's are:  $g_0 = 1\Omega$ ,  $g_1 = 1.6703$  F,  $g_2 = 1.1926$  h,  $g_3 = 2.3661$  F,  $g_4 = 0.8419$  h, and  $g_5 = 1.9841\Omega$  (Ref. 1)

### 3.1.3 Bandpass Transformation

For transformation from the LPPT to the BP circuit, the standard mapping function

$$\frac{\omega'}{\omega_1} = \frac{1}{w} \left( \frac{\omega}{\omega_0} - \frac{\omega_0}{\omega} \right) \quad (3.4)$$

is used, where

$$w = \frac{\omega_2 - \omega_1}{\omega_0} \equiv \frac{\Delta\omega}{\omega_0} = \text{fraction bandwidth} \quad (3.5)$$

$\omega_2, \omega_1$  = upper and lower band edge frequencies in the BP frequency range

$$\omega_0 = \sqrt{\omega_2 \omega_1} = \text{band center frequency} \quad (3.6)$$

so that a series inductance branch in the LPPT is transformed into a series resonant branch, whereas a shunt capacitance branch in the LPPT is transformed into a shunt resonant branch. The resonance frequency of all these branches is  $\omega_0$ , given by Eq. (3.6). That is, the LPPT in Fig. 3-1 is transformed to the BP circuit shown in Fig. 3-2.

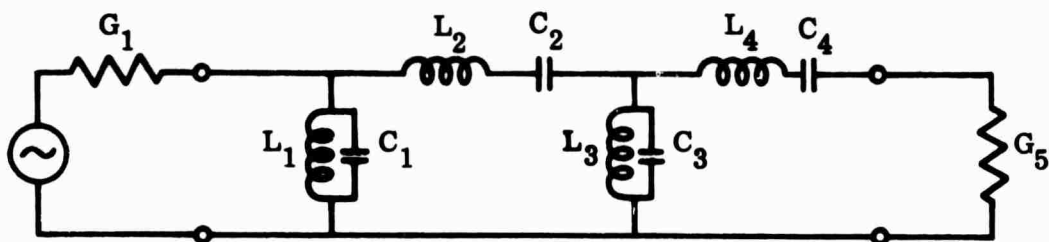


Fig. 3-2 A Bandpass Filter Circuit After Transformation From Low-Pass Prototype Circuit. The resonance frequency  $\omega_0$  of the resonant branches is given by  $\omega_0 = 1/\sqrt{L_j C_j} = \sqrt{\omega_2 \omega_1}$ , where  $j = 1$  to 4. The actual values of  $L_j$  and  $C_j$  depend on the scaling factors for  $\omega'_1$ ,  $g_0$ ,  $w$ ,  $\omega_2$ , and  $\omega_1$

#### 3.1.4 Physical Realization of the BP Network

It is recognized that at microwave frequencies the lumped-element circuit represented by Fig. 3-2 cannot be realized simply because of the distributed nature of the circuit elements. Several techniques exist for the approximation of these elements; Matthaei's technique (Refs. 3, 4, 5) will be used in this work. Since many different microwave structures can be used to realize the BP circuit approximately, it is necessary to narrow our discussion of the BP in terms of a structure. The capacity-loaded interdigital line (CLIL) filter circuit, shown in Fig. 3-3, is selected for the discussion and analysis, since it is the structure desired for the modulator.

It can be shown through transmission line analysis (Refs. 1, 5), that an equivalent circuit of the CLIL shown in Fig. 3-3 is as shown in Fig. 3-4. Ideally, the circuit shown in Fig. 3-4 must equal that shown in Fig. 3-2 at all frequencies. However, it has been found more convenient to relate the circuit in Fig. 3-4 directly to the LPPT shown in Fig. 3-1. This is done by splitting the LPPT and the equivalent circuit for the CLIL into end and interior sections. In order to allow unequal terminating admittance (i.e.,  $g_0 \neq g_5$  in Fig. 3-1), the admittance transformation has to be effected in the BP, which demands  $n \geq 4$  (as mentioned in section 3.1.2). A resonance condition is imposed on the CLIL sections to relate the circuit parameters within the CLIL. The

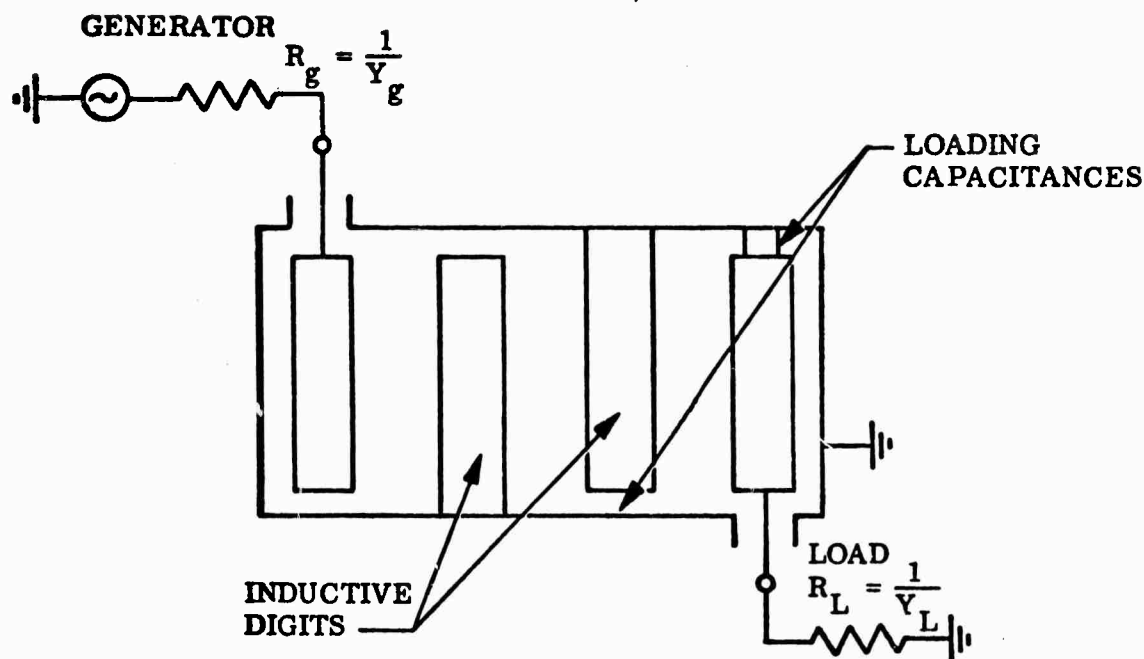


Fig. 3-3 The Strip-Line Capacity-Loaded Interdigital Line Filter, Together With Its Generator and Load

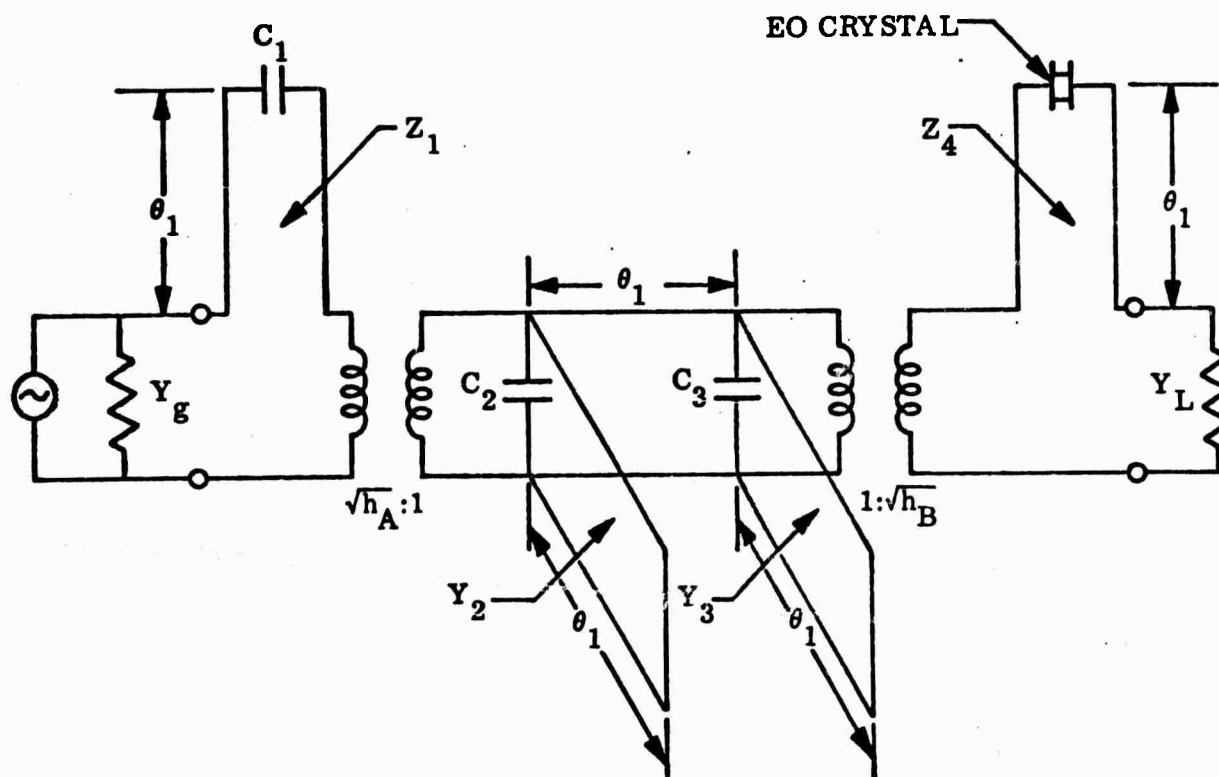


Fig. 3-4 An Approximate Equivalent Circuit for the Four-Element Capacity-Load Interdigital Line Filter

image admittances\* and phases of the CLIL interior sections at  $\omega = \omega_0$  and  $\omega = \omega_1$  are forced to agree with those of the LPPT interior sections at  $\omega' = 0$  and  $\omega' = -\omega_1'$ , respectively. For the end sections, the reactances and susceptances at  $\omega = \omega_0$  and  $\omega = \omega_1$  for the CLIL are made to agree with those for the LPPT at  $\omega' = 0$  and  $\omega' = -\omega_1'$ , respectively. By going through this forced-matching procedure, a set of design equations has been obtained (Refs. 1, 5).

Therefore, once the LPPT circuit elements are obtained by specifying  $L_{Ar}$  for maximum voltage across the crystal, a BP-CLIL can be obtained by using the design equations mentioned. The result of using the design equations is to relate the CLIL elements  $C_1, C_2, \dots, Z_1, Y_2, \dots$ , etc., to the known LPPT elements (the g's). The values obtained for the C's and Z's can be related to actual conductor dimensions, spacings, gap width, etc., by a set of charts published by Getsinger (Ref. 6).

### 3.1.5 Relationship Between Attenuation Ripple and RF Voltage at the EO Crystal

Throughout this discussion, it has been implied that a relationship between the attenuation ripple  $L_{Ar}$  and the rf voltage  $V_{rf}$  has been obtained. Discussion of this relationship has been deferred until now because it is more illustrative when discussed in terms of the CLIL equivalent circuit and the LPPT circuit rather than in terms of the LPPT circuit alone.

Consider the output section of the CLIL equivalent circuit shown in Fig. 3-5. At mid-band frequency, the output section is a series-resonant circuit, with the load impedance  $R_L$  acting as the damping element of the resonant circuit. The rms circulating current at resonance  $i_o$  is related to the power dissipation at  $R_L$  by

$$i_o = \sqrt{P/R_L} \quad (3.7)$$

---

\*The image admittance of a two-port network is defined as follows: Given a two-port network N, if admittances  $Y_{I1}$  and  $Y_{I2}$  are such that with  $Y_{I2}$  terminating Port No. 2, one sees an input admittance  $Y_{I1}$  at Port No. 1, and vice versa,  $Y_{I1}$  and  $Y_{I2}$  are the image admittances of N. In general,  $Y_{I1} \neq Y_{I2}$ .

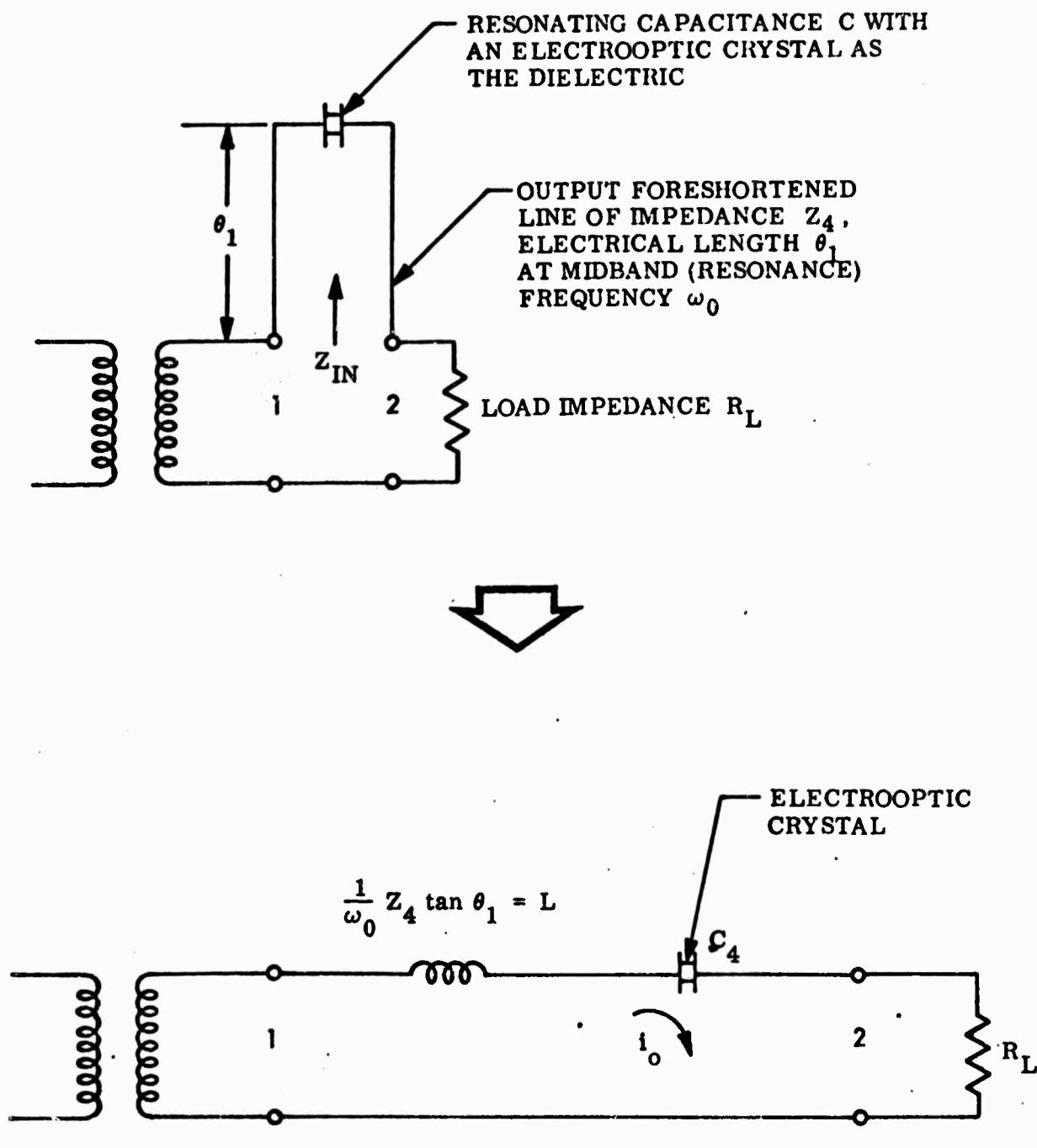


Fig. 3-5 Approximate Equivalent Circuits of the Output Section of the Capacity-Loaded Interdigital Modulator. The electrooptic crystal serves as the resonating capacitance for the inductive length of the line

The peak rf voltage across the crystal  $V_{rf}$  is then given by

$$V_{rf} = \sqrt{2} i_o Z_4 \sin \theta_1 = \sqrt{2P} Z_4 \sin \theta_1 / \sqrt{R_L} \quad (3.8)$$

where  $Z_4$  is the characteristic line impedance of the output section. Clearly, to increase  $V_{rf}$ , the factor  $Z_4 \sin \theta_1 / \sqrt{R_L}$  should be increased as much as possible.

For an EO crystal of given size, the resonating capacitance  $C$  is fixed. The resonating condition then fixes the inductance  $Z_4 \tan \theta_1$ , i.e.,  $Z_4 \tan \theta_1 = \text{constant} = \omega_0 L$

$$\therefore Z_4 \sin \theta_1 = Z_4 \tan \theta_1 \cos \theta_1 = \omega_0 L \cos \theta_1 \quad (3.9)$$

which has its maximum at  $\theta_1 = 0^\circ$ . This condition is obviously impractical, since it demands that  $Z_4 \rightarrow \infty$  so that  $Z_4 \tan \theta_1$  remains constant. In practice, one would therefore strive to make  $Z_4$  as large as practical (i.e., make the conductor as thin as practical) to allow a small value of  $\theta_1$ , contingent upon the allowable crystal size. For  $\theta_1 < 45^\circ$ , this optimization may reach the state of diminishing returns.

On the other hand, if  $R_L$  is decreased,  $V_{rf}$  increases quite rapidly. Again,  $R_L$  cannot be arbitrarily decreased since it is related to the circuit matching and bandwidth. To understand this, it is instructive to consider, first, the LPPT circuit as a matching network to the load at terminal plane 22 in Fig. 3-1, consisting of an inductance  $g_4 = L_4$  and a conductance  $g_5 = G_5$ . From Bode's relationship (Ref. 7), it can be deduced that

$$\int_0^\infty \ln \left| \frac{1}{\Gamma} \right| d\omega \leq \frac{\pi}{G_5 L_4} = \frac{\pi}{g_4 g_5} \quad (3.10)$$

where  $\Gamma$  is the reflection coefficient looking into terminal plan 11 in Fig. 3-1. This equation defines the best match that can be obtained over the entire frequency range;



i.e., the area under the  $\ln |1/\Gamma|$  versus  $\omega$  curve is constant. Thus, one can either spoil the match (large  $|\Gamma|$ , small  $\ln |1/\Gamma|$ ) to obtain poor power transfer over a large frequency range, or obtain a good match (small  $|\Gamma|$ , large  $\ln |1/\Gamma|$ ) over a small frequency range.

From Eq. (3.10), it is clear that the parameter defining the "goodness" of the match is  $1/g_4 g_5$ . Therefore, for  $n$ -element filters and matching networks, since one is interested in a "good" match over a frequency range of  $\omega' = 0$  to  $\omega' = \omega'_1$ , a "goodness parameter" decrement  $\delta$ , defined as

$$\delta = \frac{1}{\omega'_1 g_n g_{n+1}} = \frac{1}{\omega'_1 g_1 g_0} \quad (3.11)$$

is frequently used as a design parameter. Since the characteristics of the match (or attenuation ripple) are completely specified mathematically [e.g., through Eqs. (3.1) and (3.2)], choice of any two of the three parameters,  $\delta$ ,  $n$ , and  $L_{Ar}$ , uniquely determines the third.

Upon transformation into BP configuration, the decrement transforms to

$$\delta = \frac{1}{wQ} = \frac{\omega_0^2 R_L C}{\Delta\omega} \quad (3.12)$$

where  $Q$  is the  $Q$ -factor of the output section and  $R_L$  and  $C$  are as defined in Fig. 3-5. From Eq. (3.8), it is clear that  $\delta$  should be small for high  $V_{rf}$ . That is, the match within the PB should be sacrificed somewhat to obtain high modulation efficiency. For the preliminary design of the modulator as a four-element Tchebyscheff filter,  $L_{Ar}$  has been increased from the usual filter design of 0.01 dB to 0.5 dB so that  $\delta$  can be reduced from 1.4 to 0.6. This corresponds to a reduction of  $R_L$  by a factor of 2.33 for the same crystal capacitance, or an increase of  $V_{rf}$  by a factor of 1.53 for the same rf drive power.

On the other hand, if the basic prototype circuit is not a filter but an optimum matching network of the Tchebyscheff type, then for  $L_{Ar} = 0.5$  dB and  $n = 4$ ,  $\delta$  is only 0.425. In this case,  $R_L$  is reduced by a factor of 3.3, or  $V_{rf}$  is increased by a factor of 1.8% for a given power.

For the preliminary modulator design, however, the Tchebyscheff filter design is used, since a good deal of information and a number of techniques exist for the filter design, transformation, and fabrication. After adequate experience has been gained with the new design to ascertain the limitations of the design theory, the optimum Tchebyscheff matching network design will be investigated further.

### 3.1.6 Example of Modulator Design

In an actual modulator design of given  $L_{Ar}$  and  $n$ , once given the generator and load admittances ( $Y_g$  and  $Y_L$  in Fig. 3-4), the variables left to the choice of the designer are the line length at midband  $\theta_1$ , the admittance scaling factors  $h_A$  and  $h_B$  (see Fig. 3-4), and a splitting factor  $d$  in the LPPT circuit. Proper choice of these parameters will result in a physically realizable structure.

For a generator admittance of  $0.02 \text{ } \Omega$  ( $50 \text{ } \Omega$ ) and a load admittance of  $0.0525 \text{ } \Omega$  ( $19 \text{ } \Omega$ , as determined by the allowable decrement), calculations have been made for various combinations of  $\theta_1$ ,  $h_A$ ,  $h_B$ , and  $d$ . One typical set of results is shown below.

$$n = 4 \quad , \quad L_{Ar} = 0.5 \text{ dB} \quad , \quad \theta_1 = 40^\circ$$

$$h_A = 0.20 \quad , \quad h_B = 0.15 \quad , \quad d = 20$$

$$Y_g = 0.02 \text{ } \Omega \quad , \quad Y_L = 0.0525 \text{ } \Omega$$

$$\frac{Z_1}{Z_g} = 3.5926 \quad , \quad \frac{Y_2}{Y_g} = 0.1919 \quad , \quad \frac{Y_3}{Y_g} = 0.1919 \quad , \quad \frac{Z_4}{Z_g} = 1.3687$$

$$C_1 = 0.6637 \text{ pF} \quad , \quad C_2 = 0.6503 \text{ pF} \quad , \quad C_3 = 0.6502 \text{ pF} \quad , \quad C_4 = 1.7420 \text{ pF}$$

Although all the numerical values in the list appear to be reasonable, there are problems in realizing this circuit. For instance,  $Z_1$ ,  $Z_2$ , and  $Z_3$  are so high that physical realization as an interdigital circuit is not possible. Other values of  $h_A$ ,  $h_B$ , and  $d$ , as well as different values of  $\theta_1$  and  $Y_L$  near  $0.05\mathcal{U}$ , do not give substantially different results. It appears that in order to obtain the required mismatch of  $L_{Ar} = 0.5$  dB, the ratio of the internal impedances of the lines to generator impedance has to be high (e.g., a factor of 3 to 5). Since the generator impedance is assumed to be  $50\ \Omega$ , the coupled-line impedances become too high to realize.

Therefore, for a realizable filter, a lower generator impedance as seen by the filter is necessary. To accomplish this will require a transformer between the generator (usually of  $50\text{-}\Omega$  impedance) and the filter; the design and fabrication of such a transformer are not difficult. With this condition in mind, a filter design having generator and load admittance of  $0.0525\ \mathcal{U}$  ( $19\ \Omega$ ) has been obtained. The various design and circuit parameters are:

$$n = 4 \quad , \quad L_{Ar} = 0.5 \text{ dB} \quad , \quad \theta_1 = 40^\circ$$

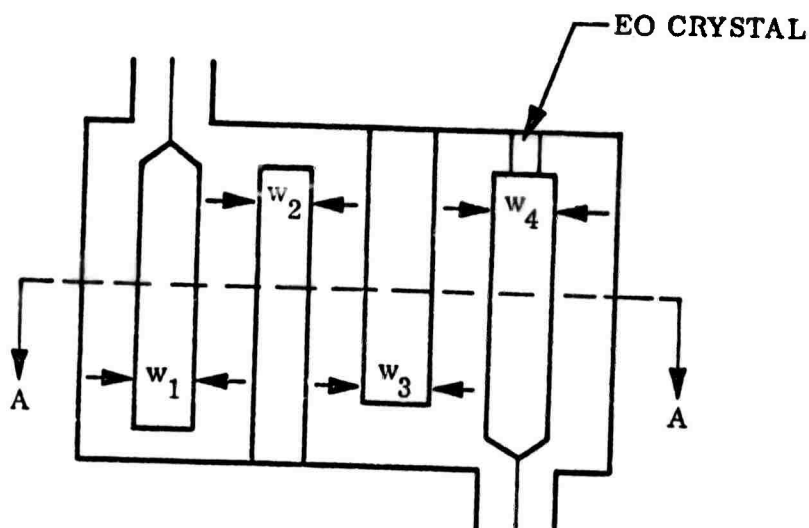
$$h_A = 0.2 \quad , \quad h_B = 0.2 \quad , \quad d = 0.65$$

$$Y_g = 0.0525\ \mathcal{U} \quad , \quad Y_L = 0.0525\ \mathcal{U}$$

$$\frac{Z_1}{Z_g} = 3.5926 \quad , \quad \frac{Y_2}{Y_g} = 0.1541 \quad , \quad \frac{Y_3}{Y_g} = 0.1541 \quad , \quad \frac{Z_4}{Z_g} = 3.5928$$

$$C_1 = 1.7422 \text{ pF} \quad , \quad C_2 = 1.6140 \text{ pF} \quad , \quad C_3 = 1.6139 \text{ pF} \quad , \quad C_4 = 1.7420 \text{ pF}$$

These values result in a realizable circuit, as shown in Fig. 3-6.



$$w_1 = 0.165$$

$$w_2 = .124$$

$$w_3 = .124$$

$$w_4 = .165$$

$$S_{12} = .075$$

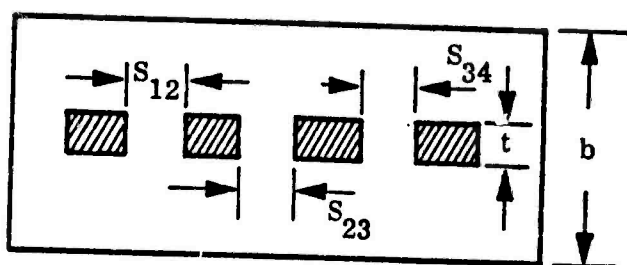
$$S_{23} = .093$$

$$S_{34} = .075$$

$$t = .120$$

$$b = .600$$

VALUES IN INCHES



SECTION AA

Fig. 3-6 An Example of a Modulator Circuit Design: Effective Generator Impedance,  $19 \Omega$ , Load Impedance  $19 \Omega$

### 3.2 INTERFEROMETRIC MODULATION STUDIES

In the interferometric mode of modulation, the modulator forms a Fabry-Perot etalon whose effective optical length is varying at the modulating signal frequency. By properly selecting and controlling the quiescent length of the modulator cavity (via temperature or dc bias), the modulator can be biased so that an rf signal applied to the electrooptic crystal will cause intensity modulation of single-mode laser radiation. Employing this form of modulation, both the light transmitted through and the light reflected back from the crystal are modulated. Either one (or both) could be used in a communication system, although the optics are simpler for the transmitted light. This modulation technique promises to be more efficient than the birefringence form and requires one less optical component, the analyzer. It does require, however, that the electrooptic crystal have higher optical quality and better surface finish; therefore, greater care must be exercised in the fabrication of these crystals.

In this mode of operation, the depth of modulation is defined as the peak-to-peak change in the light intensity (at the fundamental frequency) divided by the cw intensity of the incident laser light. That is, changing from full laser power to zero represents 100% modulation. This definition is chosen because it corresponds to the conventional "depth of modulation" definition for the birefringence modulation at quarter-wave optical bias. Modulation depth and its linearity are functions of the bias, the cavity length, the reflectivity of the etalon mirrors, and the rf voltage applied. The inter-relationship is sufficiently complex and nonlinear to warrant evaluation on a digital computer.

The computer analysis is based on a model of an ideal electrooptic crystal having the same dimensions and electrooptic coefficients as those of the crystals used in the laboratory. The purpose of the analysis was to indicate what sort of performance could be expected under ideal conditions and to provide the information necessary to decide what reflection coefficients would give the best results. Basically, as the reflection coefficients are increased, the number of partial waves having significant

amplitudes increases. Because of the finite propagation time of each partial wave within the modulating crystal, the rf modulation impressed on each partial wave will be the time average during this propagation time. The modulation will be shifted in phase from that on the previous partial wave. For higher reflection coefficients, less rf power is required to attain the same depth of modulation, but at the same time, more distortion and phase delay are produced in the modulation. The computer runs have been set up to show the tradeoffs between these quantities.

Computer runs for  $\text{LiNbO}_3$  crystals, of dimensions 0.5 by 0.5 by 5 mm and 0.5 by 0.5 by 7 mm having various reflectivities, have been made for the modulation of 0.6328- $\mu\text{m}$  light at various rf drive levels. Some of the results (for 0.5 by 0.5 by 5 mm, at 5-W drive) have been included in the First Quarterly Report. Another sample of the calculation is included in Tables 3-1 and 3-2 for the case of 0.5 by 0.5 by 7 mm crystal modulating 0.6328- $\mu\text{m}$  light. The reflectivities and crystal dimensions used correspond to actual experimental conditions. Results indicate that the reflected beam has a greater depth of modulation but possesses higher harmonic distortion and phase deviation than the corresponding transmitted beam.

The choice of crystal surface reflectivity for use in a given communication system depends critically on the tolerance of the system to harmonic distortion and phase deviation. Higher reflectivity will produce greater depth of modulation, but the analysis shows that the harmonic distortion and phase deviation increase more rapidly than the depth of modulation. Another important factor influencing this choice is the number of times that the light must reflect within the crystal (the number of partial waves) to produce a given modulation depth. Higher reflectivity results in more partial waves to produce the modulation. Since the crystals that have been obtained are not truly homogeneous and the faces are not exactly flat and parallel, the wavefront of light is distorted with each pass within the crystal. The laboratory tests on these crystals indicate that this distortion will be the limiting factors for interferometric modulation, limiting the maximum useful reflectivity.

Table 3-1

TRANSMISSION MODULATION CHARACTERISTICS OF 0.5 BY 0.5 BY  
7 mm LiNbO<sub>3</sub> CRYSTAL AT VARIOUS DRIVE POWER LEVELS.  
REFLECTIVITIES OF CRYSTAL SURFACES 0.3250, 0.2628

Modulation Frequency (GHz)  Drive Power (W)	1.0	1.25	1.5	1.75	2.0
Depth of Modulation (%)					
1	28.0	27.0	25.7	24.2	22.5
2	38.3	37.0	35.4	33.4	31.1
5	54.9	53.4	51.5	49.1	46.2
10	67.0	65.6	64.4	62.9	60.7
20	74.9	73.4	72.2	71.6	70.8
Harmonic Distortion (%)					
1	0.3	0.3	0.3	0.3	0.2
2	0.6	0.6	0.6	0.5	0.5
5	1.5	1.6	1.6	1.4	1.3
10	2.7	2.9	2.8	2.6	2.3
20	5.0	5.4	5.4	5.1	4.6
Phase Deviation From Average (deg)					
1	0.2	0.3	0.2	-0.1	-1.1
2	0.2	0.3	0.2	-0.1	-1.0
5	0.3	0.1	0.1	-0.1	-0.6
10	0.7	0.1	-0.3	-0.2	-0.1
20	1.6	1.1	-0.1	-1.1	-1.3

Table 3-2

REFLECTION MODULATION CHARACTERISTICS OF 0.5 BY 0.5 BY  
7 mm  $\text{LiNbO}_3$  CRYSTAL AT VARIOUS DRIVE POWER LEVELS.  
REFLECTIVITY OF CRYSTAL SURFACES 0.3250, 0.2628

Modulation Frequency (GHz)  Drive Power (W)	1.0	1.25	1.5	1.75	2.0
Depth of Modulation (%)					
1	30.6	30.8	30.6	30.1	29.3
2	41.9	42.2	42.1	41.6	40.6
5	60.0	60.8	61.3	61.1	60.2
10	73.2	74.8	76.7	78.4	79.2
20	81.9	83.6	86.0	89.2	92.4
Harmonic Distortion (%)					
1	0.4	0.5	0.5	0.4	0.4
2	0.9	1.0	1.0	0.9	0.8
5	2.3	2.5	2.5	2.4	2.2
10	4.3	4.7	4.6	4.2	3.7
20	8.2	9.3	9.2	8.2	7.1
Phase Deviation From Average (deg)					
1	-1.8	-1.2	-0.1	1.1	2.2
2	-1.8	-1.2	-0.2	1.1	2.3
5	-1.8	-1.3	-0.3	1.2	2.6
10	-1.4	-1.4	-0.6	1.0	3.4
20	-0.4	-0.4	-0.5	0.1	2.0



Computer results showed that for a reflectivity of 0.35 the approximation of using only two round-trip reflections within the crystal yielded a modulation depth that was only 3.2% below that for a very large number of reflections. For a reflectivity of 0.5, four round-trip reflections were required for a result that was within 1.5% of that for a very large number of reflections. For this reason, a reflectivity in the range of 0.3 to 0.35 was judged best for currently available crystals.

The high index of refraction of the  $\text{LiNbO}_3$  crystals ( $\sim 2.2$ ) gives the uncoated crystals a surface reflectivity of 0.14 in the visible. One round-trip reflection (two partial waves) within the crystal produces modulation that is within 3.5% of that for many reflections. Five crystals of dimensions 0.5 by 0.5 by 7 mm were measured in the laboratory and produced depths of modulation of 20 to 30% with 5 W of drive power. The computer analysis predicted a 35% modulation depth, so there is reasonable agreement between the analysis and the measured results. Within the group of five crystals, the static reflection curve varied and crystals having the lower reflection ratio produced the smaller depth of modulation.

Two of the above five crystals were selected for coating with 0.3 to 0.35 reflectivity in the visible for further experimentation. The coating operations, performed simultaneously on both crystals, did not produce equal reflectivities on each end: the measured reflectivity of one surface was 0.26; of the other, 0.32. Experimental results showed that for a 2-W drive, a modulation depth of 30% is obtainable for the transmission mode. This compared well with a theoretical value of about 35%. (See Table 3-1.) However, as the drive power is increased, further crystal heating, which results in greater distortion of the crystal and consequently of the interferometer configuration, causes the interfering wavefronts to distort considerably. To date, no substantial increase in modulation depth has been obtained at drive levels greater than 2 W. Experimental work to further investigate this problem is now in progress.

It should be emphasized that these tests employing larger crystals (having a cross section of 0.5 by 0.5 mm<sup>2</sup>) were made at 0.6328  $\mu\text{m}$  purely for convenience of checking against the theory. At a later date, when better quality smaller crystals are

obtained, they will be reflection coated to give the proper reflectivity at  $1.06\ \mu\text{m}$  for testing at  $1.06\ \mu\text{m}$ . At present, the optical quality of the crystals is the practical limitation, and the fabrication techniques must also be improved to yield better crystals. Further experimentation will indicate the realistic limits on the reflectivities that can be used.

### 3.3 ELECTROOPTIC/THERMAL CONTROL CIRCUIT

With the interferometric type of modulation, adjustment of the optical bias point cannot be effected by means of an optical compensator, since the change of the optical length has to occur inside the reflecting surfaces of the crystal. Control of the crystal temperature to change the crystal length may be used, but that alone is not fast enough to respond to the microwave power fluctuations that normally occur. To respond to such fluctuations, an electronic circuit, which combines the electrooptic effect with thermal control to provide continuous automatic control of the optical bias point, was devised. The electrooptic effect is used to provide fast, short-term control; the temperature is used to provide long-term control. Such a circuit has been designed, built, and tested.

A schematic view of the controller for use with interferometric modulation is shown in Fig. 3-7. The compensating electric field on the crystal is derived from two photodiodes, one of which samples the laser beam after passing through the modulator and other samples a reference beam. The diodes are electrically loaded so that, at the desired optical bias point, the two beams produce equal signals from the diode circuits. During operation, the difference between the two signals (representing a deviation from the desired bias point) is amplified by a differential amplifier followed by a high-voltage stage. The high-voltage stage is capable of applying a nominal  $\pm 300\ \text{V}$  to the modulator crystal and can follow transients with time constants of several milliseconds. This circuit provides good "instantaneous" control of the bias point.

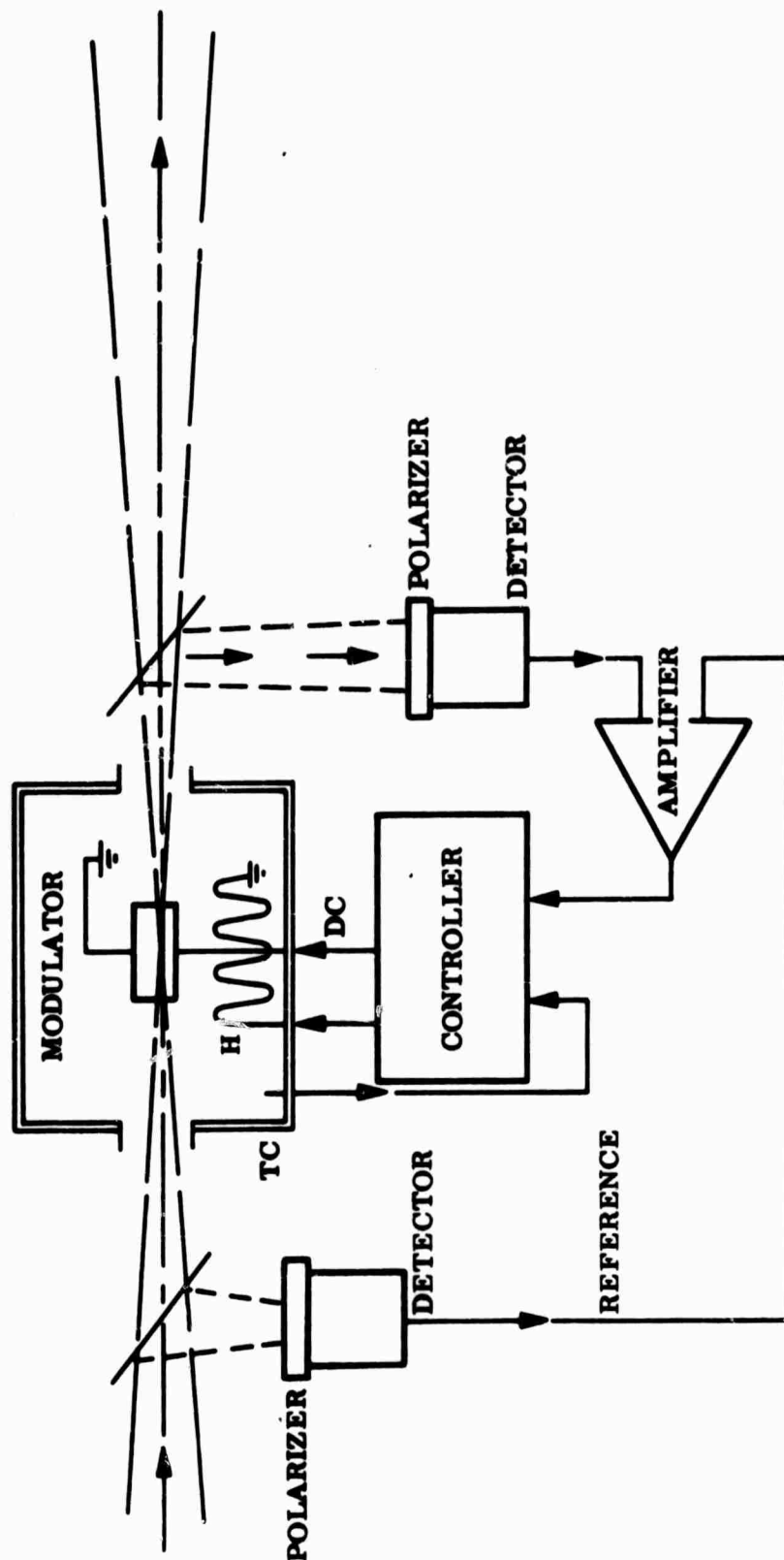


Fig. 3-7 Block Diagram of the Automatic Electrooptical Bias Scheme. The two detectors and associated polarizers monitor the amount of energy in the reference beam and the beam at the output of the modulator. Shift of optical bias from the predetermined value will result in a change in the energy content in the beam, causing an error signal. The error signal activates the controller to give a dc-compensating voltage and a change in heater power to maintain correct optical bias

Since it is observed that a high bias electric field on the crystal will cause a certain amount of beam distortion, the compensating field should always approach zero in its quiescent state. This is accomplished by using this crystal bias voltage to actuate the crystal-oven heater control circuit so as to change the oven temperature to make the bias voltage approach zero. The crystal temperature will then vary to the necessary temperature to maintain proper bias. Since the thermal time constant of the oven is a few seconds, thermal control is relatively slow. Under these conditions, if the fluctuation in microwave power is strong, it is still possible for the oven temperature to become too high or too low. For this reason, the oven temperature is monitored while it is being controlled by the crystal bias voltage, and if the temperature goes outside a predetermined range of operation, the oven control is automatically switched to a thermistor probe for a period of time. After the temperature has had time to center itself in the operating range, the control is automatically switched back to the crystal bias voltage. This circuit has successfully kept the oven temperature within a reasonable operating range for a variety of changing laboratory conditions.

While the oven heater is controlled by the crystal bias voltage, the temperature could go into slow oscillations, which would prevent stable operation. This is due to the fact that there is a long time delay before the crystal reacts to any thermal change in the oven heater. To stabilize the oven temperature, both the first and second derivatives of the temperature are combined with the optical bias voltage to provide an error signal for the oven heater. With such an error signal, the heater is electrically damped so that the temperature cannot change at a rate too fast for the crystal to follow. Future modulator structures can be designed with tighter thermal coupling between the heater and crystal for improved bias control. However, the present construction has been satisfactory for achieving automatic compensation for long periods of time.

### 3.4 EVALUATION OF EFFICIENT CRYSTALS

#### 3.4.1 Static Evaluation

Although it was anticipated that good-quality, efficient crystals such as barium sodium niobate would become available for this study, no crystal was obtained until late in the second quarter: one each of barium sodium niobate and strontium barium niobate. Unfortunately, the optical quality of these crystals is still rather poor, as can be seen in Fig. 3-8. Figure 3-8a is the extinction pattern for barium sodium niobate, and Fig. 3-8b is that for strontium barium niobate. It appears that the fringes observed across the apertures of these crystals are due mainly to the strains induced during crystal fabrication, although some intrinsic problems such as crystal non-uniformity and striations are also present.

#### 3.4.2 Dynamic Tests in a Modulator

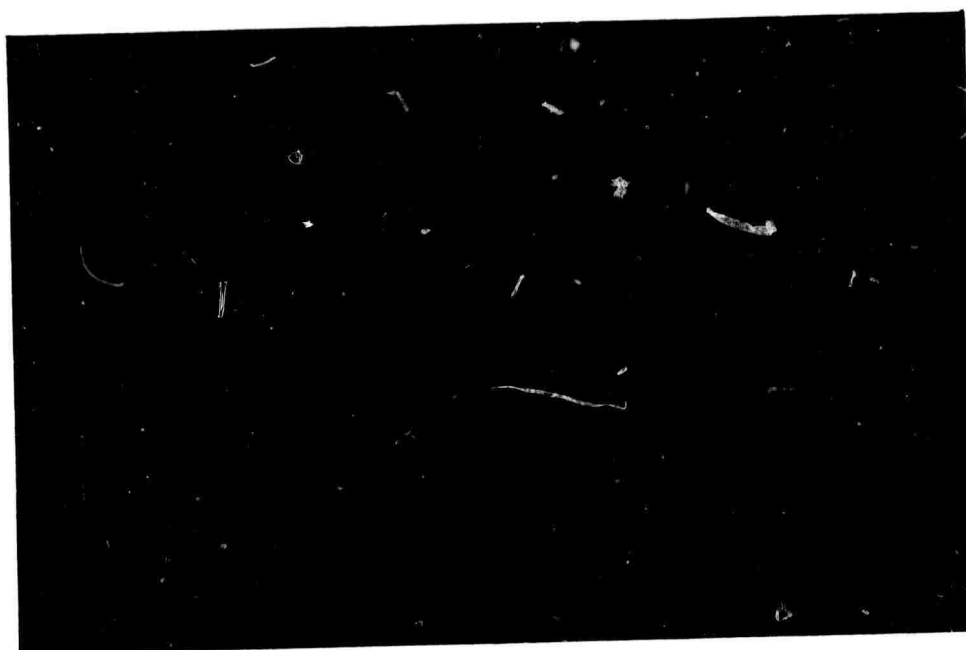
With the quality as it is, there is not much hope that the crystals will perform very well in the interferometric mode. Consequently, the barium sodium niobate crystal is being tested for birefringence modulation. The results obtained so far have been discouraging. At 2-W drive level, 28% modulation depth, as compared with a theoretical 55%, is the best obtainable. This low modulation index is probably due to the crystal quality, as can be seen from Fig. 3-8. Additional tests are being performed to determine the modulation depth more exactly. No measurements on strontium barium niobate have yet been made. Efforts to obtain better quality crystals are continuing.

### 3.5 CRYSTAL DAMAGE AND BEAM PROFILE STUDIES

It is well known that shorter wavelength radiations induce more optical damage in the form of inhomogeneities in refractive indexes than longer wavelength radiations in crystals such as lithium niobate. Tests have been made on  $\text{LiNbO}_3$  crystals, 0.3 by 0.3 by 7.0 mm, in a modulator using the output of an argon laser consisting of several



(a) Extinction Pattern for Barium Sodium Niobate



(b) Extinction Pattern for Strontium Barium Niobate (SBN 50-50)

Fig. 3-8 Extinction Patterns for Finished Electrooptic Crystals (apertures approximately 0.3 by 0.4 mm). Three different optical biases are shown

lines in the 0.4880–0.5145  $\mu\text{m}$  range, totaling about 3/4 W of optical power. If the crystal does not suffer from damage at these wavelengths, there will be no problem in operating at 1.06  $\mu\text{m}$  using the same optical power. At 180°C, up to 700 mW of optical power between 0.4880 and 0.5145  $\mu\text{m}$  was focused to 80- $\mu\text{m}$  diameter through the crystal, corresponding to a power density of 14  $\text{kW}/\text{cm}^2$ , without any observable damage. The far-field pattern of the transmitted beam was scanned using a pinhole, and the results are presented in Figs. 3-9, 3-10, and 3-11 for beams under various conditions.

Figure 3-9 shows the laser beam profile before it passes through any optics; Fig. 3-10 shows the beam profile after passing through a focusing lens alone; and Fig. 3-11 shows it after passing through both the lens and the crystal. Most of the disturbance of the beam is due to the lens as the result of the multiple reflection occurring between the non-AR-coating lens surfaces. A comparison of Figs. 3-10 and 3-11 shows that insertion of the crystal causes little change. Figure 3-11 also shows that no significant deviation from a Gaussian profile results from the passing of the beam through both lens and crystal at power levels up to 700 mW, which was the full output of the laser used.

It was concluded that there would be no optical damage problem with 1.0 W of 1.06- $\mu\text{m}$  radiation focused through this type of crystal, so long as it was maintained at 180°C.

Preliminary tests were also run on a sample of strontium barium niobate (60% Sr to 40% Ba). After irradiation using 0.4880 and 0.5145  $\mu\text{m}$  at power densities up to 9  $\text{kW}/\text{cm}^2$ , the crystal showed brownish discoloration which faded away slightly after removal of the radiation. However, annealing at high temperatures did not remove the discoloration, but rather changed its position. It was suggested by the vendors that the discoloration was due to slight inclusion of platinum during growth and poling. No further experiments were made on this sample. No beam profile measurement was made, since the sample was not optically polished.

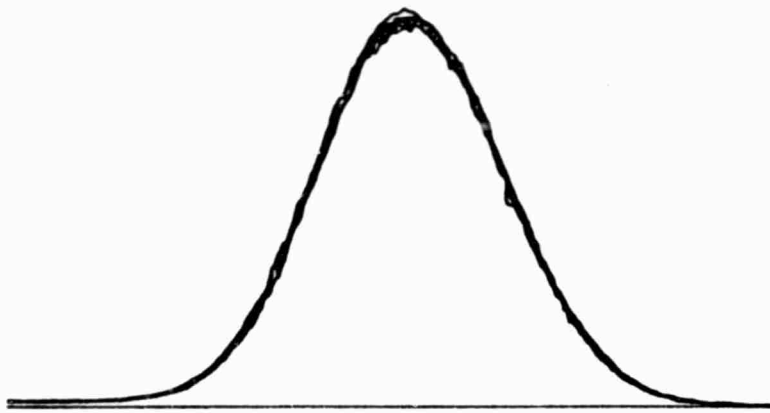


**Fig. 3-9 Measured TEM<sub>00</sub> Far-Field Beam Profile of an Argon Laser Output Showing the Gaussian Distribution**

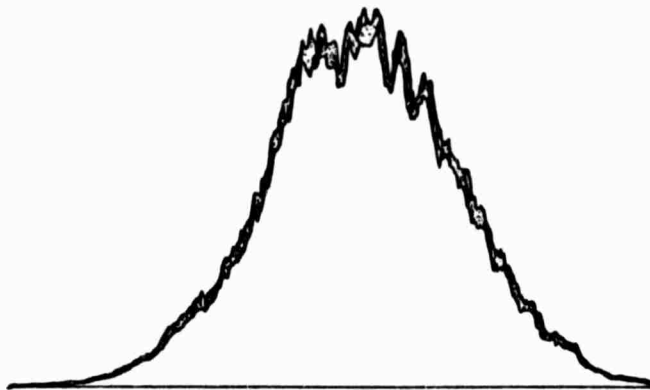


**Fig. 3-10 Measured Far-Field Beam Profile of an Argon Laser Output After Passing Through an Uncoated Focusing Lens**

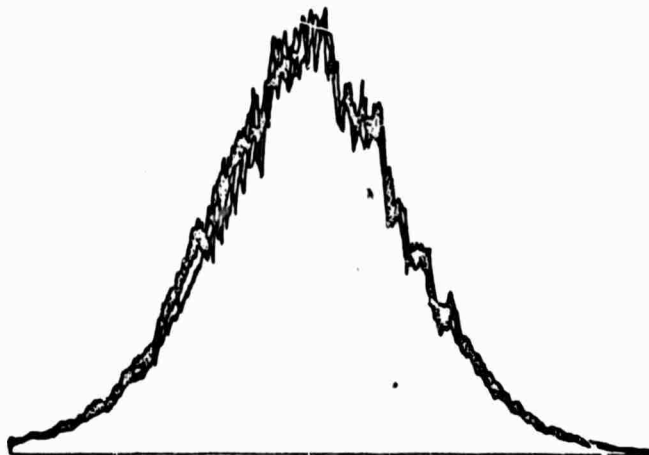


**Fig. 3-11 Measured Far-Field Beam Profile of an Argon Laser Output After Passing Through the Uncoated Focusing Lens and a LiNbO<sub>3</sub> Crystal**



It has also been informally reported that  $\text{LiNbO}_3$ , after being operated in air at elevated temperatures (e.g.,  $180^\circ\text{C}$ ) for a period of time, becomes yellow. It had been speculated that this discoloration was due to the gradual loss of oxygen atoms, under heat, from the crystal structure. The experience in our laboratory, with  $\text{LiNbO}_3$  operating in air at  $180^\circ\text{C}$  for over a year, does not support this observation. However, to ascertain that such problem will not occur when operating in vacuum, tests were run in the laboratory by heating a 5 by 5 by 5 mm sample of  $\text{LiNbO}_3$  in a vacuum bell jar while monitoring its transmission at  $0.6328\ \mu\text{m}$ . After 23 hr at about  $200^\circ\text{C}$ , and then 3 hr at  $350^\circ\text{C}$ , no decrease in transmission was observed. In addition, the transmission of the crystal from  $0.25$  to  $1.2\ \mu\text{m}$  was also measured in a Cary Model 14 spectrophotometer before and after the vacuum test; no degradation in transmission, especially near the absorption edge at  $0.3$  to  $0.4\ \mu\text{m}$ , was observed. Since the shift in absorption edge is a very sensitive measure of yellowing, it is concluded that under our test conditions, no degradation in optical transmission is observed.

### 3.6 FUTURE PLANS

Future work on the optical modulator development will proceed in the direction described in the following paragraphs.

#### 3.6.1 Modulator Circuit Study

Further analysis of the circuit will be continued to arrive at a final design. If transformers have to be used, as appears to be the case, Tchebyscheff transformers will be designed for the proper ratio. The circuit will be fabricated and tested.

#### 3.6.2 Modulation Study

Both interferometric and birefringence modulation will be studied further. The interferometric case entails more careful measurements of the  $\text{LiNbO}_3$  crystals having  $\sim 30\%$  reflectivity; the birefringence modulation study will be concentrated on newer crystals, such as  $\text{Ba}_2\text{Na}(\text{NbO}_3)_5$  and  $\text{Sr}_{0.5}\text{Ba}_{0.5}(\text{NbO}_3)_2$ .

### **3.6.3 Beam Distortion Study**

Since the newer crystals obtained are of such inferior quality, additional beam distortion studies (of beam profile, scattering, etc.) will be conducted.

Section 4  
REFERENCES

1. G. L. Matthaei et al., Microwave Filters, Matching Networks and Coupling Structures, McGraw-Hill, New York, 1964
2. S. Gussow and G. Weathers, Computer-Aided Filter Design Manual, NASA SP-3049, Contract NAS 8-20055, Sperry Rand Corporation, Huntsville, Ala., 1969
3. G. L. Matthaei, "Design of Wide-Band (and Narrow-Band) Band-Pass Microwave Filters on the Insertion Loss Basis," IRE Trans. Microwave Theory & Tech., Vol. MTT-8, Nov 1960, pp. 580-593
4. G. L. Matthaei, "Interdigital Band-Pass Filters," IRE Trans. Microwave Theory & Tech., Vol. MTT-10, Nov 1962, pp. 479-491
5. G. L. Matthaei et al., Microwave Filters and Coupling Structures, Final Report, SRI Project 3527, Contract DA 36-039 SC87398, Stanford Research Institute, Menlo Park, Calif., Feb 1963
6. W. J. Getsinger, "Coupled Rectangular Bars Between Parallel Plates," IRE Trans. Microwave Theory & Tech., Vol. MTT-10, Jan 1962, pp. 65-72
7. H. W. Bode, Network Analysis and Feedback Amplifier Design, D. Van Nostrand, New York, 1945